Measuring mechanical stress in living tissues

Manuel Gómez-González[1,6]✉, *Ernest Latorre*[1,2,6], *Marino Arroyo*[1,2]✉ and *Xavier Trepat*[1,3,4,5]✉

Abstract | Living tissues are active, multifunctional materials capable of generating, sensing, withstanding and responding to mechanical stress. These capabilities enable tissues to adopt complex shapes during development, to sustain those shapes during homeostasis and to restore them during healing and regeneration. Abnormal stress is associated with a broad range of pathological conditions, including developmental defects, inflammatory diseases, tumour growth and metastasis. A number of techniques are available to measure mechanical stress in living tissues at cellular and subcellular resolution. 2D techniques that map stress in cultured cell monolayers provide the highest resolution and accessibility, and include 2D traction force microscopy, micropillar arrays, monolayer stress microscopy and monolayer stretching between flexible cantilevers. Mapping stresses in tissues cultured in 3D can be achieved using 3D traction force microscopy and the microbulge test. Techniques for measuring stress in vivo include servo-null methods for measuring luminal pressure, deformable inclusions, Förster resonance energy transfer tension sensors, laser ablation and computational methods for force inference. Although these techniques are far from becoming everyday tools in biomedical laboratories, their rapid development is fostering key advances in our understanding of the role of mechanics in morphogenesis, homeostasis and disease.

[1]*Institute for Bioengineering of Catalonia (IBEC), Barcelona Institute of Science and Technology (BIST), Barcelona, Spain.*

[2]*LaCàN, Universitat Politècnica de Catalunya-BarcelonaTech, Barcelona, Spain.*

[3]*Centro de Investigación Biomédica en Red en Bioingeniería, Biomateriales y Nanomedicina, Barcelona, Spain.*

[4]*Unitat de Biofísica i Bioenginyeria, Universitat de Barcelona, Barcelona, Spain.*

[5]*Institució Catalana de Recerca i Estudis Avançats (ICREA), Barcelona, Spain.*

[6]*These authors contributed equally: Manuel Gómez-González, Ernest Latorre.*

✉*e-mail: mgomez@ibecbarcelona.eu; marino.arroyo@upc.edu; xtrepat@ibecbarcelona.eu*

https://doi.org/10.1038/s42254-020-0184-6

Adherent animal cells are able to generate mechanical stresses to move, divide, remodel and sense their mechanochemical microenvironment. The generation and transmission of stresses in a tissue can give rise to collective cellular phenomena of different levels of complexity, from the relatively simple contraction of striated muscle to the intricate folding of an epithelium. The role of mechanical stresses in biological systems is particularly apparent in early development, when cellular layers of different identity undergo pronounced 3D movements to shape tissues[1]. However, living tissues are mechanically active throughout life. For example, the intestinal epithelium self-renews every 3–5 days through a series of mechanical functions, such as division, migration and extrusion[2,3]. Mechanical stresses also have a crucial role in wound healing, where they enable cell migration towards the wound and supracellular contraction to seal it[4]. Conversely, aberrant stresses mediate devastating diseases, such as myopathies and cancer[5,6]. Unlike in passive materials, stresses in living tissues are transduced by cells to trigger and regulate biological responses[7]. For example, an increase in tension causes cell proliferation, whereas a decrease induces cell extrusion[8–10].

A number of tools have been developed to measure mechanical stress over multiple length scales, from the single molecule to the entire organ. Here, we review technologies to measure stress in tissues at cellular and subcellular resolution. Because our focus is on stress, we exclude technologies that are used to measure other relevant mechanical quantities, such as stiffness, viscoelasticity or poroelasticity. Therefore, we do not discuss magnetic tweezers[11,12], optical tweezers[13,14], acoustic tweezers[15], atomic force microscopy[16], micropipette aspiration[17], microindentation[18], microplate actuators[19], Brillouin microscopy[20,21] or tissue dissection and relaxation[22]. The reader is referred to excellent recent reviews on these techniques[23–34].

In this Review, we first discuss fundamental concepts in continuum mechanics, which might be familiar to most physicists and engineers but not to the broad biomedical community interested in tissue mechanobiology. Next, we discuss the techniques that have been developed to measure tissue stress in vitro and ex vivo, starting with the techniques that are applicable to 2D cell cultures, such as 2D traction force microscopy (TFM), micropillar arrays, monolayer stress microscopy (MSM) and tensile tests of cultured tissues. We then introduce methods that are used to measure tissue stress in 3D cultures, including 3D TFM and the microbulge test. Finally, we discuss techniques that are compatible with in vivo

Key points

- Mechanical stresses generated by cells determine the fate, form and function of living tissues.
- Several techniques have been developed to measure tissue stress at subcellular resolution.
- State-of-the-art technologies now enable high-resolution mapping of time-varying stress fields in 2D and 3D cell cultures.
- Measuring stresses in vivo remains an outstanding challenge that is currently addressed through the combination of image-based computational modelling and the insertion of soft inclusions in tissues of interest.

measurements, such as servo-null methods, inclusions, Förster resonance energy transfer (FRET) tension sensors, laser ablation and force inference. Throughout, we provide examples of applications of these techniques and discuss their strengths and limitations.

The concept of stress and traction

A force is an interaction that tends to deform an object or change its velocity. Forces acting on any material can be classified as internal or external. For a cell in a tissue, internal forces are generated by subcellular components, such as the actomyosin cytoskeleton, whereas external forces are exerted by the surrounding extracellular matrix (ECM) or neighbouring cells. However, the mechanics of deformable continuum materials is not formulated in terms of force but, rather, in terms of force per unit area, a physical quantity known as stress. The need for the concept of stress is clear from the fact that the same force applied over a smaller area will cause a different deformation than if applied over a larger area of a material.

The force per unit area acting on any internal or external surface of a material is called the traction vector $\boldsymbol{T}$. It is assumed that the traction vector depends only on the location within the material and on the unit normal vector $\boldsymbol{n}$ to the surface (Cauchy's stress postulate). Therefore, the traction vectors that act on opposite sides of a surface are equal in magnitude and opposite in sign (Newton's third law of motion) (BOX 1). In general, because the traction vector is not perpendicular to the surface, it consists of normal $\boldsymbol{t}_n$ and tangential $\boldsymbol{t}_t$ vector components. Normal traction vectors can be compressive (negative) or tensile (positive), depending on their sign relative to $\boldsymbol{n}$ (BOX 1).

As there are infinitely many surfaces passing through a point A, there are also infinitely many traction vectors acting on that point. Therefore, to fully characterize the stress state of a tissue, we introduce the stress tensor field $\boldsymbol{\sigma}(A)$, a second-order mathematical entity that contains all the stress information at a given point A. It can then be proved that the traction vector $\boldsymbol{T}$ depends in a linear way on $\boldsymbol{n}$:

$$\boldsymbol{T} = \boldsymbol{n} \cdot \boldsymbol{\sigma}(A). \quad (1)$$

At any point A, the stress tensor $\boldsymbol{\sigma}(A)$ is a 3×3 symmetrical matrix (BOX 2), which can adopt distinct forms, depending on the geometry of the material and the loading conditions. We illustrate the most characteristic of such forms in BOX 3, using the process of blastocyst implantation as an example.

Force balance in a tissue is defined by Newton's second law of motion. For a tissue in equilibrium modelled as a continuum material and ignoring inertial forces, Newton's second law of motion is expressed in terms of the stress tensor as (see BOX 4 for the derivation):

$$\nabla \cdot \boldsymbol{\sigma} = -\boldsymbol{b}, \quad (2)$$

where $\nabla\cdot$ indicates the divergence operator, which, when applied to the stress tensor, produces a vector expressing the out-of-equilibrium force density in the material, and where $\boldsymbol{b}$ is an externally applied force density. When there are no external forces applied to the system (that is, $\boldsymbol{b}=\boldsymbol{0}$), the internal stresses are balanced at every point and the divergence in Eq. 2 is identically zero. The above equilibrium equation, together with its boundary conditions, governs the mechanics of the system. In 3D, $\boldsymbol{\sigma}$ has six independent components and the equilibrium (vector) equation only provides three independent equations. In 2D, where stress is sometimes referred to as tension, $\boldsymbol{\sigma}$ has three independent components and equilibrium provides two independent equations. To have a closed problem, extra conditions, termed constitutive equations, are needed. Constitutive equations model the stress-generation mechanisms of the material under consideration, and, for a living tissue, they may include elastic (relating stress and deformation), viscous (relating stress and deformation rate) and active (involving internal consumption of chemical energy) components. The simplest of these relations is provided by isotropic linear elasticity, which relates $\boldsymbol{\sigma}$ and the deformation in a linear way through two coefficients: Young's modulus E and Poisson's ratio ν. Constitutive equations of higher complexity are used when elasticity is not applicable, invoking viscosity[35], hyperelasticity[36], superelasticity[37], plasticity[38], viscoelasticity[34], poroelasticity[39] or polarity[40]. For some specific cases with highly symmetrical geometries, such as an expanding cell monolayer or a spherical dome, the stress can be fully determined without specifying the constitutive equation by simply invoking equilibrium[37,41].

Techniques for measuring stress in 2D

Biological tissues display considerable variability in their geometrical and mechanical configuration (BOX 3). For example, individual leukocytes crawl on 2D surfaces and invade the 3D ECM during an inflammatory response; epithelial cell monolayers cover the internal and external surfaces of the human body, often withstanding a 2D plane stress (BOX 2); the early mammalian embryo behaves as a thin-walled spherical vessel under pressure; and a tumour is a 3D material subjected to compressive stress due to its growth and to stromal forces. Each of these systems displays different mechanical states and, thus, requires different techniques to measure the generated stresses. Below, we discuss techniques developed to measure stress in living tissues and their range of applicability (summarized in TABLE 1).

2D TFM

TFM is the first technique developed to measure the tractions exerted by single cells and tissues on soft elastic substrates. The initial implementation of TFM showed that single cells are able to wrinkle a thin, soft silicon

Box 1 | **The traction vector**

The figure is a geometric representation of the traction vector, $\boldsymbol{T}$ (red), acting at point *A* of a body subject to external forces (green arrows).

A given body can be cut by an infinite number of imaginary planes passing through a point *A*. Each cut will define two sub-bodies and a pair of surfaces with outer normal vectors $\boldsymbol{n}$ and $-\boldsymbol{n}$ (see the figure). The traction vector $\boldsymbol{T}$ is defined as the force between these adjacent surfaces divided by their surface area and is linearly related to the stress tensor and to the normal vector by Cauchy's stress theorem (Eq. 1). As the traction vector can have any direction relative to the surface, it is conveniently decomposed into normal ($\mathbf{t}_n$, indicating compression or tension) and tangential ($\mathbf{t}_t$, indicating shear) vector components:

$$\mathbf{t}_n = (\boldsymbol{T}\cdot\boldsymbol{n})\,\boldsymbol{n} = (\boldsymbol{n}\cdot\boldsymbol{\sigma}\cdot\boldsymbol{n})\,\boldsymbol{n}, \quad (10)$$

$$\mathbf{t}_t = \boldsymbol{T} - \mathbf{t}_n = \boldsymbol{n}\cdot\boldsymbol{\sigma} - (\boldsymbol{n}\cdot\boldsymbol{\sigma}\cdot\boldsymbol{n})\,\boldsymbol{n}. \quad (11)$$

Normal tractions can be tensile (pulling), when they point in the direction of the outer normal $\boldsymbol{n}$, or compressive (pushing), when they point in the opposite orientation. In traction force microscopy, the surface of interest where tractions are defined is the interface between cells and the ECM.

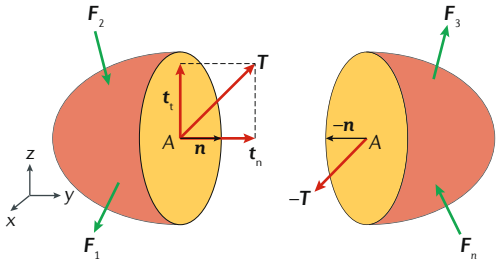

rubber substrate to which they are adhered[42]. Subsequent improvements attempted the quantification of the tractions underlying such deformations by modelling the substrate as a flat, thin membrane under plane stress[43–45]. Following these seminal contributions, the technique was reformulated to its current implementation, 2D TFM, which measures the 2D tractions exerted by cells on flat substrates of known thickness[46]. Typical substrates include polyacrylamide and soft polydimethylsiloxane gels, which are transparent, tunable in stiffness and can be coated with ECM proteins. 2D TFM has been used in numerous studies to directly measure the displacements that cells generate on the upper surface of the substrate to which they are adhered[47,48]. These displacements are measured relative to a reference state, which is typically obtained by detaching all the cells from the substrate and, thus, relaxing it to its non-deformed configuration (FIG. 1a,b). Displacements are entirely caused by the tractions that cells exert on the substrate and they are computed by the imaging (using light microscopy) of fiducial markers that are embedded in the substrate or attached to its surface. Recent implementations of 2D TFM eliminate the need to image the relaxed configuration by distributing the markers into a regular array that serves as a theoretical reference[36,49].

Different strategies are available to obtain the tractions that cause the measured surface displacements. In all cases, mechanical equilibrium (Eq. 2; BOX 4) is imposed for the substrate, and a constitutive behaviour is chosen to establish a closed problem. The substrate is commonly considered uniform and isotropic, and its constitutive behaviour is typically assumed to be linear elastic, with a known Young's modulus *E* and Poisson ratio *v*. 2D TFM can be used when the out-of-plane tractions exerted by the sample tissue are negligible compared with the in-plane tractions, yielding a 2D traction vector on the substrate surface[50].

By also assuming a simple geometry (such as a half-space or a finite-thickness substrate) and small displacements (infinitesimally smaller than any relevant dimension of the gel), several computational methods have been developed to obtain the tractions. These methods take advantage of linear superposition and of the availability of analytical forms for the Green's function of the problem, which provides the displacement field in the substrate under the action of a point surface load. In most cases, tractions are calculated as the solution to an inverse problem, typically computed in Fourier space to accelerate computational performance[50,51]. In some applications, the inversion can also be performed in real space using the boundary element method[46]. Regardless of the specific computational formulation, the inverse problem is mathematically ill posed, and because of the long-ranged decay of the Green's function, the computed tractions are very sensitive to small variations or noise in the displacement data. This difficulty can be mitigated by using either regularization techniques during the solution of the inverse problem[52,53] or Bayesian methods[54]. When the previous hypotheses do not hold, for example, when the substrate is not uniform because there is a gradient of stiffness (*E*), when the geometry of the substrate is complex or when there are large displacements, then tractions need to be computed from the displacements using the finite element method (FEM)[55].

A different strategy is to directly compute the substrate deformation from the spatial derivatives of the displacement field[56]. The stress tensor $\boldsymbol{\sigma}$ is then directly computed from the deformation using the constitutive equation of the substrate material. Finally, the traction vector is obtained simply as $\boldsymbol{T} = \boldsymbol{n}\cdot\boldsymbol{\sigma}$. The main shortcoming of this approach is the noise in the displacement field, which arises from optical-microscopy limitations, resolution of image-analysis algorithms and material heterogeneities of the substrate. Noise in the measurements is strongly amplified when calculating the displacement derivatives, and the calculated $\boldsymbol{\sigma}$ might not satisfy the equilibrium Eq. 2.

TFM has been pivotal in the emergence and growth of the field of mechanobiology. At the single-cell level, TFM made visible for the first time the tractions that cells exert when they migrate[46], divide[57] and otherwise mechanically interact with their environment[58,59]. At the tissue level, TFM has been used to establish how cells coordinate local traction generation during collective cell migration[60], how mechanical waves propagate in a cell monolayer[61] and how cells combine different motility modes in wound healing[4]. Other discoveries enabled by TFM include collective durotaxis[62] (collective migration up an ECM stiffness gradient), kenotaxis[63] (collective polarization of cellular traction forces) and cell jamming[64] (transition from fluid-like to solid-like collective behaviour). Although most TFM experiments have been performed using cultured cell

Box 2 | **The stress tensor**

The figure is a geometric representation of the stress tensor $\boldsymbol{\sigma}$ at point *A* of a body under a load ***F***.

As there are an infinite number of planes cutting through a point *A*, there are an infinite number of traction vectors ***T*** acting on that point. However, the stress state at point *A* is completely defined by six orthogonal planes infinitely close to *A* (defining an infinitesimal cube centred in *A*) and their associated tractions (see the figure, part **a**). In equilibrium, the traction vectors in parallel faces are equal and opposite and, therefore, only three traction vectors, $\boldsymbol{T}^{(x)}$, $\boldsymbol{T}^{(y)}$ and $\boldsymbol{T}^{(z)}$, are needed to describe the stress state at point *A*. For any given coordinate system, the components of these three traction vectors (see the figure, part **b**) can be organized in a 3×3 matrix called the stress tensor $\boldsymbol{\sigma}$, which is symmetrical, owing to the balance of angular momentum:

$$\boldsymbol{\sigma} = \begin{bmatrix} \sigma_{xx} & \sigma_{xy} & \sigma_{xz} \\ \sigma_{xy} & \sigma_{yy} & \sigma_{yz} \\ \sigma_{xz} & \sigma_{yz} & \sigma_{zz} \end{bmatrix}. \tag{12}$$

As a result of the spectral theorem, an orthonormal coordinate system can always be found for which the matrix is diagonal (see the figure, part **c**):

$$\boldsymbol{\sigma} = \begin{bmatrix} \sigma_1 & 0 & 0 \\ 0 & \sigma_2 & 0 \\ 0 & 0 & \sigma_3 \end{bmatrix}. \tag{13}$$

When $\boldsymbol{\sigma}$ has a diagonal form, its three independent values (its eigenvalues) are called principal stresses ($\sigma_1 \geq \sigma_2 \geq \sigma_3$). When the principal stresses are equal, the stress state is called hydrostatic or spherical, and in any orthonormal coordinate system, $\boldsymbol{\sigma}$ is proportional to **1**, the identity 3×3 matrix. For example, fluids at rest have a uniform (independent of *A*) stress state of the form:

$$\boldsymbol{\sigma} = -p \cdot 1 = \begin{bmatrix} -p & 0 & 0 \\ 0 & -p & 0 \\ 0 & 0 & -p \end{bmatrix}, \tag{14}$$

where *p* is the pressure. In this situation, the traction vector ***T*** is always parallel to ***n*** and, thus, perpendicular to any surface (the tangential component of the traction is identically zero) and compressive of magnitude *p*.

In a general case, the stress tensor $\boldsymbol{\sigma}$ can always be decomposed into its spherical or hydrostatic part (which produces tractions perpendicular to any surface) and its remaining deviatoric part:

$$\boldsymbol{\sigma} = \boldsymbol{\sigma}^{\mathrm{sph}} + \boldsymbol{\sigma}^{\mathrm{dev}}, \tag{15}$$

$$\boldsymbol{\sigma}^{\mathrm{sph}} = \frac{1}{3}\left(\sigma_{xx} + \sigma_{yy} + \sigma_{zz}\right) \cdot 1 = \sigma_m \cdot 1 = \begin{bmatrix} \sigma_m & 0 & 0 \\ 0 & \sigma_m & 0 \\ 0 & 0 & \sigma_m \end{bmatrix}, \tag{16}$$

$$\boldsymbol{\sigma}^{\mathrm{dev}} = \boldsymbol{\sigma} - \boldsymbol{\sigma}^{\mathrm{sph}} = \begin{bmatrix} \sigma_{xx} - \sigma_m & \sigma_{xy} & \sigma_{xz} \\ \sigma_{xy} & \sigma_{yy} - \sigma_m & \sigma_{yz} \\ \sigma_{xz} & \sigma_{yz} & \sigma_{zz} - \sigma_m \end{bmatrix}. \tag{17}$$

The deviatoric part, which is represented as a traceless matrix, is responsible for the shear stresses.

When modelling thin objects, such as plates placed parallel to the (*x*–*y*) plane, it may be justified to assume that the traction vector normal to the top and bottom free surfaces of the plate is identically zero and that the stress tensor does not depend on *z*. As the normal vector to those surfaces is parallel to the *z*-direction, the stress tensor takes the form:

$$\boldsymbol{\sigma} = \begin{bmatrix} \sigma_{xx} & \sigma_{xy} & 0 \\ \sigma_{xy} & \sigma_{yy} & 0 \\ 0 & 0 & 0 \end{bmatrix}. \tag{18}$$

These conditions are referred to as plane stress. In these conditions, the stress state becomes two-dimensional, and an interaction of the thin plate with a substrate (for example, a measured traction between a cell monolayer and its substrate) becomes a body force rather than a surface traction (see Eqs. 4 and 5).

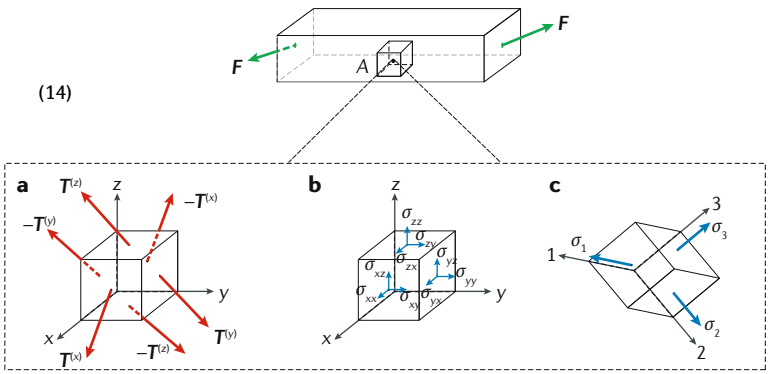

monolayers, the technique has also been applied to tissue explants[65].

Key advantages of TFM over other techniques include the straightforward implementation, the potential application at different scales and the considerable versatility of the method, which has enabled the use of TFM in physics and engineering problems[48], such as wetting[35,66], fracture[67,68] or adhesion[69–71], in both living and inert materials. A major disadvantage of TFM is that retrieving the tractions from the displacements is an ill-posed problem and, thus, is very sensitive to experimental noise. Furthermore, 2D TFM is, by definition, restricted to measuring tangential in-plane tractions, but deformations on flat gels might be due to out-of-plane tractions, resulting in errors in the traction field measured with 2D TFM[72,73].

Micropillar arrays

The use of micropillar arrays to measure tractions exerted by a tissue is conceptually similar to TFM, but the continuous flat-gel substrate is substituted with a discrete array of slender, vertical micropillars of micrometre-sized cross section, typically fabricated with polydimethylsiloxane[74]. Because of the localized nature of adhesion to the substrate, micropillar arrays measure an integrated traction over a small region (that is, a net force). Micropillars are physically anchored at the base and are free at the tip, in a vertical-cantilever-beam configuration. Cell attachment is restricted to the top surface of the micropillar, which defines the area of force application (FIG. 1c,d). The in-plane component of the forces applied on the substrate can be calculated from the displacements of the micropillar tips. Owing to

the inherent locality and discreteness of the mechanical problem, the implementation of the technique is mathematically and computationally simpler than TFM. For deflections much smaller than the micropillar length, the applied net force and tip displacement are linearly related by the elastic spring equation:

$$F = \left(\frac{3EI}{L^3}\right)\delta, \quad (3)$$

where F is the applied force, I is the moment of inertia, L is the length of the micropillar and δ is the measured displacement. Equation 3 is only valid for slender pillars with a length greater than 10 times their radius and of uniform cross section.

Micropillar arrays are microfabricated following a regular lattice, which provides a reference from which deflection can be calculated. Particle-tracking software is used to find the centroid of each tip, and its location is compared with the theoretical position of the pillar in the ideal lattice. According to Eq. 3, the substrate stiffness and stiffness gradient sensed by the cells can be modified by tuning the pillar material, length[74] and/or cross section[75]. A variant of this technique uses only two thick vertical micropillars[76,77]. Contractile cells, such as fibroblasts[76] and cardiomyocytes[76,77], are seeded between them, surrounded by ECM proteins, mimicking a 3D microtissue. Because the pillars are not slender and their cross section is not uniform, their response is not linear as in Eq. 3, and, thus, their force–deflection curve needs to be experimentally calibrated.

Micropillar arrays have been used to quantify forces during single and collective cell migration[4,74,78], yielding force patterns that are comparable to those reported with TFM. In static monolayers, micropillar arrays have been used to study the tangential forces involved in neutrophil transmigration through the endothelium[79]. This technique has also been used to study the role of

Box 3 | **The stress tensor in biological tissues**

The figure is a schematic of different representative stress states that are present during embryo implantation.

The stress tensor $\boldsymbol{\sigma}$ is, in general, a 3×3 symmetrical full matrix, in which all normal and tangential elements are non-zero (see the figure, part **a**). However, for specific geometries and loading conditions, the matrix will adopt simplified forms. Here, we illustrate some characteristic mechanical configurations by using the process of blastocyst implantation as an example[207].

The inner cell mass (see the figure, part **a**) is a 3D body in a 3D stress state, and, therefore, $\boldsymbol{\sigma}$ is, in general, a 3×3 full matrix. By contrast, the blastocoel (see the figure, part **b**) is a fluid-filled cavity in a 3D hydrostatic state, and, thus, $\boldsymbol{\sigma}$ is a 3D diagonal matrix with equal diagonal elements. The endometrium (see the figure, part **c**) is a flat monolayer in a state of plane stress. Therefore, $\boldsymbol{\sigma}$ can be reduced to a full 2D matrix, with both normal and tangential components. Conversely, the wall of the blastocyst, termed the trophectoderm (see the figure, part **d**), is in a state of capillary (surface) tension, owing to the internal pressure exerted by the blastocoel. $\boldsymbol{\sigma}$ is then reduced to a 2D diagonal matrix with equal diagonal components. Finally, the endothelial surface of a blood capillary is subjected to a combination of shear stress, hydrostatic pressure and surface tension. $\boldsymbol{\sigma}$ can then be expressed as a sum of two matrices, one with only shear components owing to blood flow and one with a more complex structure due to the vessel geometry, hydrostatic pressure and surface tension, generally expressed in cylindrical coordinates (see the figure, part **e**).

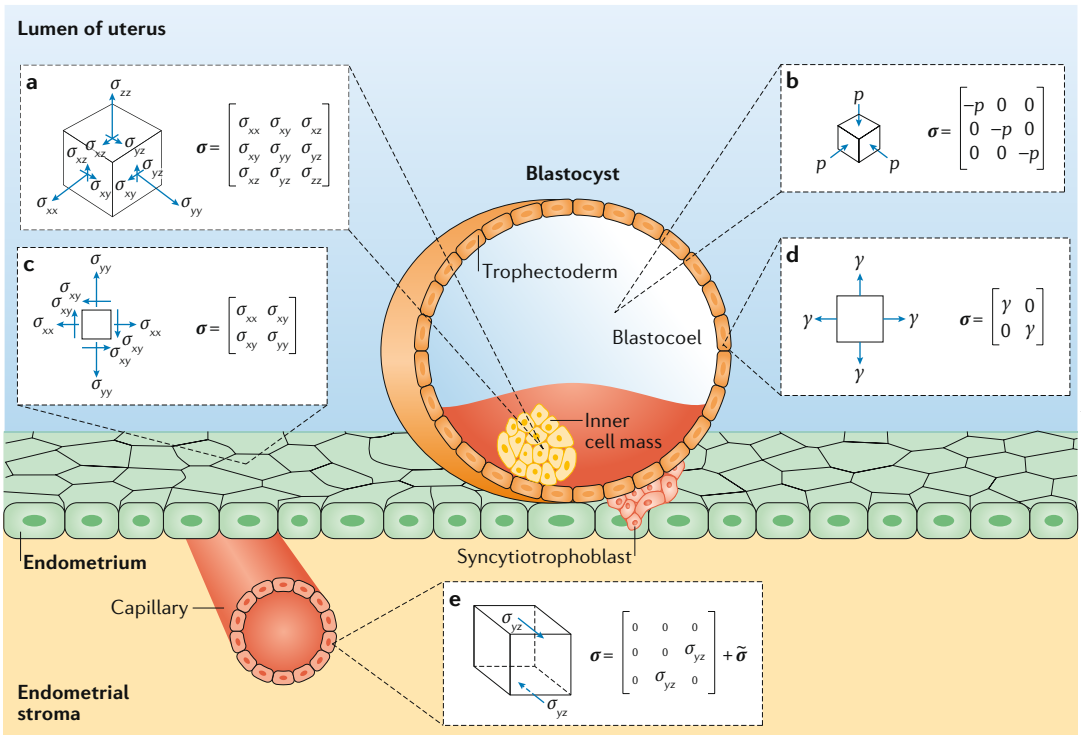

Box 4 | **Equilibrium equation for a continuum**

The resultant $\boldsymbol{R}$ of all external forces applied on a sub-volume V of a tissue bounded by the surface S is the sum of all surface forces acting on its boundary and of all body forces acting on its volume:

$$\boldsymbol{R} = \int_S \boldsymbol{T}\,\mathrm{d}S + \int_V \boldsymbol{b}\,\mathrm{d}V = \int_S \boldsymbol{\sigma}\cdot\boldsymbol{n}\,\mathrm{d}S + \int_V \boldsymbol{b}\,\mathrm{d}V = \int_V (\nabla\cdot\boldsymbol{\sigma} + \boldsymbol{b})\,\mathrm{d}V, \tag{19}$$

where the last step was obtained by invoking the divergence theorem. Newton's second law of motion can then be written as:

$$\boldsymbol{R} = \int_V (\nabla\cdot\boldsymbol{\sigma} + \boldsymbol{b})\,\mathrm{d}V = \int_V \rho\boldsymbol{a}\,\mathrm{d}V. \tag{20}$$

where $\boldsymbol{a}$ is the acceleration and ρ is the mass density. Despite the fact that tissues are dynamic systems that change over time, we can assume that they relax instantly to their closest state of mechanical equilibrium[186]. In this approximation, the tissue is said to be in a quasi-equilibrium state, which, since the sub-volume is arbitrary, results in equilibrium Eq. 2:

$$\int_V (\nabla\cdot\boldsymbol{\sigma} + \boldsymbol{b})\,\mathrm{d}V = 0 \Rightarrow \nabla\cdot\boldsymbol{\sigma} = -\boldsymbol{b}. \tag{21}$$

When there are no body forces acting on a tissue (that is, $\boldsymbol{b} = \boldsymbol{0}$), the internal stress gradients balance themselves at each point of the tissue:

$$\nabla\cdot\boldsymbol{\sigma} = 0. \tag{22}$$

tractions in wound healing[4] and to elucidate the role of leading cells in collective cell migration[80]. Modifying the geometrical properties of the micropillars, such as the length and cross-sectional shape, was used to show that cells increase the force generated as pillar stiffness is increased[81] and elongate in the direction of highest stiffness[75]. This approach has also been employed to study the link between rigidity sensing of the environment and cancer-cell growth[82].

Compared with 2D TFM, micropillar-array-based traction microscopy has the advantage of providing a direct local interpretation of the relationship between applied force and pillar deflection. Tracking the displacements of the pillars is simpler than following patterns of bead markers, and cells do not need to be detached to capture a reference image, given that the reference position of the pillars is calculated from an ideal grid. Furthermore, the mathematical and computational methods to calculate the forces are straightforward. Finally, stiffness gradients can be created in the substrate by varying the shape of the pillars, rather than their material properties. However, micropillar arrays have some drawbacks, mostly associated with the discrete nature of the adhesion of cells to the pillars. Indeed, micropillar arrays provide topological cues that affect cell behaviour and, even when the substrate is correctly functionalized, cells still tend to centre the empty spaces between pillars. The requirement for very slender micropillars poses microfabrication and handling challenges. Furthermore, it is only possible to measure in-plane displacements of the micropillar tips and, thus, vertical tractions are disregarded. Given that the actual relaxed position of the micropillars might deviate from their location in the ideal grid, the use of a theoretical reference image introduces random noise in the deflection measurement and, therefore, in the force calculation. Finally, the presence of a deformable substrate under the pillars has been reported to induce an overestimation of the tractions applied by the tissues under study, consequently requiring the introduction and validation of correction factors[83].

MSM

Given the traction field exerted by a tissue on a flat substrate and invoking simple force-equilibrium arguments and mechanical assumptions, it is possible to calculate the internal stress distribution in the tissue (FIG. 1e,f). This approach, generally known as MSM, was first developed to measure the average internal stress in a single cell[41] and was then applied to measure the internal-tension distribution in an expanding cell monolayer[60], cell doublets[84,85], triplets[86] and larger clusters of cells[87].

In MSM, the cell monolayer is modelled as a very thin, flat plate under plane-stress conditions[88,89]. In this 2D setting, the equilibrium Eq. 2 takes the form (BOX 4):

$$\frac{\partial\sigma_{xx}}{\partial x} + \frac{\partial\sigma_{xy}}{\partial y} = \frac{T_x}{h}, \tag{4}$$

$$\frac{\partial\sigma_{xy}}{\partial x} + \frac{\partial\sigma_{yy}}{\partial y} = \frac{T_y}{h}, \tag{5}$$

where σ_{xx}, σ_{yy} and σ_{xy} are the components of the stress tensor in the tissue, h is the mean height of the monolayer, and T_x and T_y are the tractions measured by 2D TFM, which, in this 2D approximation, replaces $\boldsymbol{b}$ in Eq. 2. These two partial differential equations are insufficient to determine the three unknown stress components and must be complemented by the Beltrami–Michell compatibility condition:

$$\left(\frac{\partial^2}{\partial x^2} + \frac{\partial^2}{\partial y^2}\right)(\sigma_{xx} + \sigma_{yy}) = \frac{1+\nu}{h}\left(\frac{\partial T_x}{\partial x} + \frac{\partial T_y}{\partial y}\right). \tag{6}$$

An implicit assumption of this equation is that the tissue displays linearly elastic isotropic behaviour. The MSM tissue stress inferred with MSM is then obtained by solving Eqs. 4–6 with suitable boundary conditions[88,89].

This approach requires knowledge of Poisson's ratio ν but not the Young's modulus E of the monolayer. An alternative approach has been proposed to calculate the monolayer internal stresses from the substrate displacements (rather than tensions) by solving the elasticity equations for the monolayer[90]. This approach has the advantage of not requiring the calculation of the tractions exerted on the substrate and allowing for non-uniformities in E and ν of the monolayer. However, uncertainties in the values of the mechanical properties of the monolayer will greatly impact the calculated tensions.

For monolayers that cannot be modelled as elastic and isotropic, Eq. 6 does not hold, and the problem is underdetermined unless a constitutive model is assumed. A Bayesian inversion method, Bayesian inversion stress microscopy, has been proposed to solve

Table 1 | **Techniques available to measure mechanical stresses in living tissues**

Technique	Measured quantity	Output	Strengths	Limitations	Refs
2D, in vitro and ex vivo methods					
2D traction force microscopy	2D displacement of the top surface of the substrate	2D traction vector	Absolute measurement; simple implementation; mechanical properties of the substrate can be tuned	Very sensitive to noise; neglects out-of-plane tractions	4,35,36,42–73
Micropillar arrays	2D displacement of the tip of the micropillar	2D traction force	Absolute measurement; no reference image is needed; clear physical interpretation of the measured force	Discrete adhesion; topography may affect cell behaviour; deformable substrate under pillars affects measurements	4,74,75,77–83
Monolayer stress microscopy	Displacement of the substrate	Local internal monolayer stress tensor	Accesses local internal stresses of the tissue	Tissue is assumed to have linear, uniform and isotropic elasticity and uniform thickness	35,40,41,60–62,84–94,204
Suspended monolayers	Cantilever displacement	Average internal monolayer stress	Stress or strain are imposed by the user	Local stress is not obtained	95–101
3D, in vitro and ex vivo methods					
2.5D traction force microscopy	3D displacement of a gel substrate	3D traction vector	3D traction can be measured	Anisotropic 3D point spread function; very sensitive to noise (high-quality measured displacements are needed); computational complexity	37,72,73,104–111
3D traction force microscopy	3D displacement of the ECM surrounding the tissue	3D traction vector	3D traction can be measured; physiologically relevant ECM	Anisotropic 3D point spread function; nonlinear material behaviour of the surrounding ECM; cells remodel and degrade ECM; computational complexity	38,103,112–118
Microbulge test (domes)	3D displacement of the substrate surface	Luminal pressure and internal stress of curved monolayer	No need to assume any constitutive behaviour for cells; accessing internal tension for curved monolayers	Only applicable to cell types that form domes	37,121
In vivo methods					
Servo-null methods (pressure gauges)	Electrical resistance at the capillary tip	Luminal pressure	Direct access to luminal interstitial pressure	Invasive; complex experimental set-up	121,128–142
Inclusions	Inclusion shape and/or deformation	Local tissue stress tensor components	Able to report 3D tissue stress	Only accesses stress value near to the inclusion; might perturb force transmission in the tissue; requires microinjection in vivo	39,143–148,156,157,205
FRET tension sensors	Fluorescence intensity	Local tension at the molecular level	Genetically encoded; local measurement	Only reports tension, not compression; calibration issues; no directional information; unclear effect of the surrounding medium and fluorophore stability	151,158–161,163–168,170
Laser ablation	Recoil velocity	Relative tissue stress	High spatiotemporal control of the perturbation; easy implementation	Invasive; relative measurements unless viscosity of the tissue is assumed	171–182
Force-inference methods	Tissue shape	Relative local internal stress	Very simple experimental implementation; non-invasive	Relative measurements only; computational complexity; highly sensitive to segmentation noise	37,183–193,195–203,206

ECM, extracellular matrix; FRET, Förster resonance energy transfer.

Eqs. 4 and 5 without the need for a constitutive model[91]. This approach, which can be interpreted as an unbiased regularization, is, in principle, devoid of free parameters and has been shown to be robust with respect to the choice of underlying statistical model.

A mathematical framework has been developed to quantify bending moments in the cell monolayer from the out-of-plane tractions exerted on the substrate[92]. The problem is decomposed into a plane MSM state (governed by Eqs. 4–6) and a bending state induced by the out-of-plane components of the traction vector[92,93].

MSM has been pivotal in describing emerging phenomena, such as plithotaxis[89] (the tendency of cells to follow the direction of maximum principal stress), active dewetting of epithelial islands[35], collective durotaxis of epithelial monolayers[62], cell extrusion at topological

defects[40] and the role of mechanical interactions between follower cells in the emergence of leaders during epithelial migration[94].

MSM has the advantage of accessing the internal stresses of a tissue, rather than the interactions of the tissue with its surrounding environment, in a non-invasive way. However, it assumes that the elastic mechanical properties of the tissue are uniform and imposes restrictive geometric constraints, such as considering a flat monolayer with uniform thickness. These limitations are absent in formulations of MSM in quasi-1D configurations, such as cell chains or monolayers expanding from

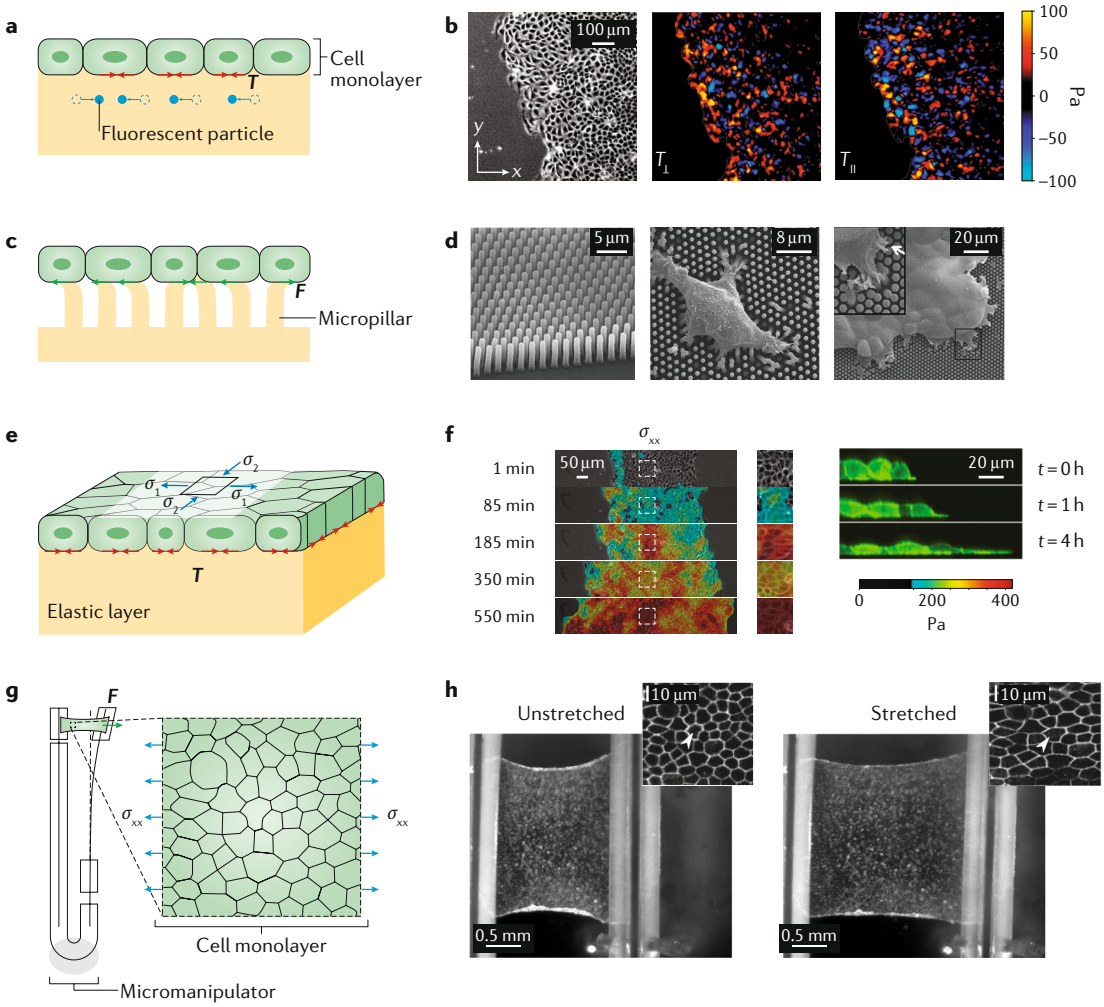

Fig. 1 | **Techniques for measuring tractions and internal stresses in 2D tissues in vitro. a** | Schematic of the principles of 2D traction force microscopy. A flat elastic gel is synthetized and cells or a tissue are allowed to attach to its surface. Cells exert tractions on the substrate, and fluorescent particles in or on the substrate are imaged using various microscopy methods, typically, confocal microscopy, allowing the resulting deformation to be tracked by comparing the position of the particles with an image of the substrate at rest (that is, after complete removal of adhered cells). Tractions are then calculated by using different computational and analytical approaches. **b** | Representative 2D traction force microscopy experiment. Phase-contrast image of a flat cell monolayer on top of a polyacrylamide gel (left), together with the tractions exerted by the cells in the directions parallel (centre) and perpendicular (right) to the advancing edge[60]. **c** | Schematic of the micropillar-array technique. Cells are seeded on top of an array of micropillars and the deflection of these pillars is proportional to the locally applied force. **d** | Representative micropillar experiment. Scanning electron micrograph of a micropillar array (left) with a single cell (centre) and a cell monolayer (right) lying on top of it[78]. **e** | Schematic of monolayer stress microscopy (MSM). In this method, the internal stresses of a flat cell monolayer can be calculated from the tractions that the monolayer applies on an elastic substrate. **f** | Representative MSM experiment. Expanding cell monolayer with overlaid colour-coded internal stresses calculated with MSM[61] (left). Side view of an expanding monolayer (right). **g** | Schematic of the suspended-monolayer method. The tensional state of a flat monolayer can be directly measured and controlled with a micromanipulator. **h** | Representative suspended-cell-monolayer experiment. Monolayer before (centre) and after (right) stretching applied with a micromanipulator[96]. The inset shows a magnified view of a region of a monolayer before and after stretching[97]. The white arrowheads indicate the same cell before and after stretching. Part **b** reprinted from REF.[60], Springer Nature Limited. Part **d** reprinted with permission from du Roure, O. et al. *Proc. Natl Acad. Sci. USA* **102**, 2390–2395 (2005)[78], © National Academy of Sciences, USA. Part **f** reprinted from REF.[61], Springer Nature Limited. Part **h** reprinted from REFS[96,97], Springer Nature Limited.

a rectangular pattern[61]. In 2D monolayers, the impact of MSM assumptions in the recovered stress field has been analysed in detail[88]. Monolayer mechanical properties are dependent on cell type and microenvironment, and might not be fully described by an elastic constitutive equation[37]. Similarly, cell monolayers might not have a uniform height. Finally, the original implementation of MSM assumes a plane-stress state, which might not be applicable to all types of monolayer, a limitation that has been partially addressed by including the bending moments of the monolayer[92].

Suspended monolayers

A direct tensile testing of in vitro and ex vivo cell cultures can be performed by using suspended cell monolayers[95]. These tensile assays enable the quantification of both the rheology of the monolayer[95] and its stress response to mechanical deformations[96]. In these experiments, a freely suspended cell monolayer is attached at one end to a rigid rod and at the other to a flexible rod, which is used as a manipulator to apply a given strain or stress and as a transducer to measure the conjugated stress or strain exerted by the monolayer[97] (FIG. 1g,h). The suspended monolayer is physically and optically accessible, enabling direct visualization of the tissue while it is being stretched.

Tensile tests of suspended cell monolayers have been used to characterize mechanical properties at the tissue, cellular and subcellular scales[95], and these experiments have been computationally simulated with vertex models[98]. Tensile tests have also been applied to study the contribution of cell division to stress relaxation and tissue homeostasis[99], with results well captured by vertex-model simulations[100]. Tensile tests have also shown that the stress response of cell monolayers to applied strains is controlled by the actomyosin cortex, both in cell monolayers grown in vitro and in multilayered explants of larval *Drosophila melanogaster* wing imaginal discs cultured ex vivo[96]. Furthermore, compression tests have been used to study the mechanoresponse of the actomyosin cytoskeleton and to identify a buckling threshold above which monolayers remain folded[101]. Finally, mechanical probing of curls formed at the edges of suspended monolayers provides a method to measure the out-of-plane internal stresses of tissues[102].

The biggest advantage of using suspended monolayers is that tensile and compression tests can be performed on a cell monolayer devoid of matrix, thus, directly testing the cellular material. Moreover, as the cell monolayer can be imaged while it is being manipulated, combining suspended monolayers with computational force-inference methods might be possible. However, the very specialized and low-throughput protocol for sample preparation and testing is a disadvantage of suspended-monolayer assays.

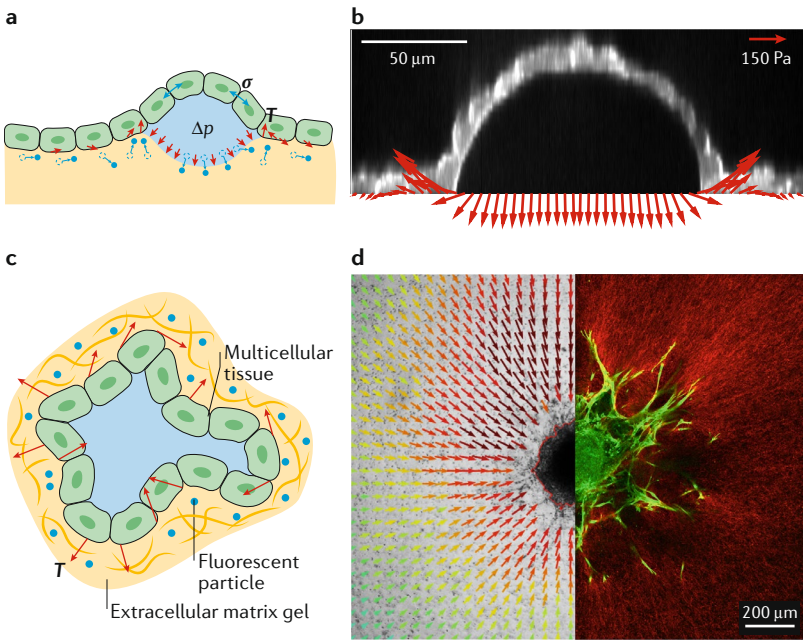

Fig. 2 | **Techniques for measuring tractions and internal stresses in 3D tissues in vitro.** **a** | Schematic of 2.5D traction force microscopy (TFM). In this technique, cells or a tissue are seeded on top of a 2D elastic substrate, and the displacements of the substrate (detected as changes in the position of the blue particles embedded in the substrate, typically by confocal microscopy) are measured in 3D. From these displacements, the 3D traction field can be calculated. For simple geometries, such as spherical caps, the internal stresses of the tissue can be recovered with a microbulge test. **b** | Representative 2.5D TFM experiment. 3D traction field (red arrows) generated by an epithelial dome (side view) on a flat substrate[37]. The magnitude of the tractions is indicated by the red scale arrow. **c** | Schematic of 3D TFM. The full 3D displacement field (red arrows) for tissues grown inside a deformable extracellular matrix gel can be measured by detecting changes in the position of matrix-embedded particle tracers by confocal microscopy, and, from this field, the full 3D traction field can be inferred. **d** | Representative 3D TFM experiment. Breast-cancer spheroid embedded in a 3D collagen I matrix. Bright-field microscopy image (left) with superimposed extracellular-matrix displacements (arrows) and fluorescent-microscopy image (right) of the spheroid (green) and matrix (red). Image part **b** reprinted from REF.[37], Springer Nature Limited. Image part **d** courtesy of N. Grummel, D. Böhringer and B. Fabry, University of Erlangen-Nuremberg, Germany.

Techniques for measuring stress in 3D

Specific techniques have been developed to measure the tractions and stresses in tissues cultured in 3D, as discussed below and summarized in TABLE 1.

2.5D and 3D TFM

2.5D TFM. It is well known that cells induce 3D displacements of the surrounding extracellular matrix by applying 3D forces[103]. Even when attached to flat surfaces, tissues exert normal forces on their substrate, which are sometimes comparable in magnitude to their in-plane counterparts[104,105]. In these cases, 2D TFM is not a valid approach and a different technique is needed. A natural extension of 2D TFM, 2.5D TFM, relaxes the hypothesis of zero normal tractions at the substrate surface and measures a 3D displacement field of the top layer of the substrate to infer the 3D traction vector field (FIG. 2a,b). To obtain 3D tractions from measured 3D displacements, the same mathematical and computational approaches for 2D TFM can be used. In the first implementation of 2.5D TFM, a uniform, isotropic and linear elastic substrate with simple geometry and small displacements was assumed, and 3D traction fields were calculated from displacements by following a direct approach and evaluating the constitutive elastic equation for the substrate[106,107]. Subsequently, a boundary-element method was proposed to generalize Dembo and Wang's solution[46], by considering an incompressible substrate

($\nu = 0.5$) and, thus, uncoupling the normal and tangential problems[108]. Alternatively, 3D traction fields can be calculated from displacements using the Fourier transform and the known Green's function for the problem[72]. For other cases, where the aforementioned hypotheses do not hold, the FEM is needed[104].

2.5D TFM has been used to elucidate the interplay between normal and tangential forces during migration of single cells[105], the influence of 3D traction stresses in the protease-dependent invasion of cancer[109] and diapedesis of leukocytes through a vascular endothelial monolayer[110]. 2.5D TFM has also been employed to simultaneously measure traction forces and the substrate's Poisson's ratio from the displacements of fiducial markers at different substrate locations[111].

The main advantage of 2.5D TFM is that it builds on 2D TFM, retaining its experimental and analytical simplicity, while qualitatively improving the scope of its measurements by correctly quantifying 3D tractions. However, 2.5D TFM also shares the main drawback of 2D TFM, which is the high sensitivity to experimental noise.

3D TFM. To study some physiological processes, such as tumour invasion or angiogenesis, it may be more pertinent to measure the tractions exerted in 3D by a tissue embedded in ECM. The quantification of a 3D traction field from a 3D displacement field, termed 3D TFM, is fundamentally more challenging from a conceptual, experimental and computational point of view (FIG. 2c,d). A central conceptual hurdle of this technique is that cells continuously synthesize and remodel their ECM and, as a consequence, it is unclear if the measured displacements are produced by the tractions exerted by the cells or if they are the result of ECM remodelling[33]. Furthermore, the prolonged 3D imaging required to capture the entire ECM surrounding the tissue might be phototoxic for the sample. In addition, the physiological ECM includes fibres and, thus, cannot be modelled as linearly elastic.

An early implementation of 3D TFM estimated the traction exerted by the invading front of a cancer spheroid embedded in a Matrigel matrix by tracking the motion of embedded microparticles[112]. Although this approach is limited by the assumption of linear elasticity, the measurement of the particle displacements in only one plane through bright-field illumination and the assumption that the traction force points in the direction of the average particle displacement, it paved the way for more sophisticated studies. To tackle some of the problems of 3D TFM, some researchers have used well-characterized viscoelastic materials, such as agarose[113], or engineered synthetic matrices that behave as linear elastic materials[114]. Other groups have characterized the nonlinear constitutive behaviour for physiologically relevant ECMs, such as collagen gels[38,115]. A simplification of 3D TFM has been applied to tumour spheroids[116]. By taking advantage of the approximately spherical geometry of the spheroids and assuming spherical symmetry of the stress state, only an equatorial plane of the spheroid and the ECM needs to be imaged. The radial far-field displacements of the ECM are measured as a function of the distance to the spheroid, and a scalar value of the tissue contractility is calculated using the FEM. In a particularly simplified implementation of 3D TFM, spherical tissues, such as cancer spheroids[117] and blastocysts[118], are encapsulated within a spherical hydrogel drop and the normal stresses exerted by the spherical tissues are inferred from changes in the radius and wall thickness of the hydrogel capsule.

3D TFM has been used to describe the invasion, in physiologically relevant conditions, of healthy[114] and disease-model cells[115]. The greatest benefit of 3D TFM is the ability to use physiologically relevant ECMs. However, the main limitation is the need to deal with nonlinear constitutive behaviours and 3D materials that can be degraded and remodelled by cells.

Both 2.5D and 3D TFM are affected by the current imaging limitations of 3D optical microscopy, such as a lower resolution in the z-plane compared with the in-plane (x–y) resolution and a decline in image quality with increasing thickness of the sample.

Microbulge test

The microbulge test is based on inducing the formation of out-of-plane domes over a soft, impermeable and elastic substrate[119]. Domes are blister-like structures that enclose a pressurized, fluid-filled lumen[120]. The cell monolayer is idealized as a structural membrane supporting two-dimensional tangential stress and uniform transepithelial pressure[121]. Bending moments and out-of-plane shear stresses are neglected, consistent with the sharp contact angle of the domes with the substrate. The luminal fluid indents the soft elastic substrate with a pressure that can be computed by applying 2.5D TFM[37] or servo-null methods[121], which both yield similar quantitative results. The fact that dome geometry is very close to a spherical cap implies that its tangential stress is uniform, isotropic and completely described by a scalar value, as in a capillary system. As a result of the axisymmetry of the system, the stress state of the dome can be fully computed by imposing mechanical equilibrium (Laplace's law[122,123]):

$$\sigma = \frac{R}{2}\Delta p, \tag{7}$$

where σ is the tangential uniform and isotropic stress, R is the dome radius (readily measured from a 3D confocal microscopy z-stack) and Δp is the lumen hydrostatic pressure.

A microbulge test has been implemented to investigate the stress state of curved epithelial monolayers[37] (FIG. 2a,b). The stress–strain relationship for the suspended and curved epithelia showed an unexpected constitutive mechanical behaviour termed active superelasticity[37], which allows tissues to undergo very large and reversible deformations at a constant tension. The plateau in tension is explained by a phase transformation between barely stretched and super-stretched cells that coexist in the epithelial dome. The phase-transformation mechanism includes cortical depletion under stretch and re-stiffening at extreme deformations to stabilize the super-stretched phase. Active superelasticity may

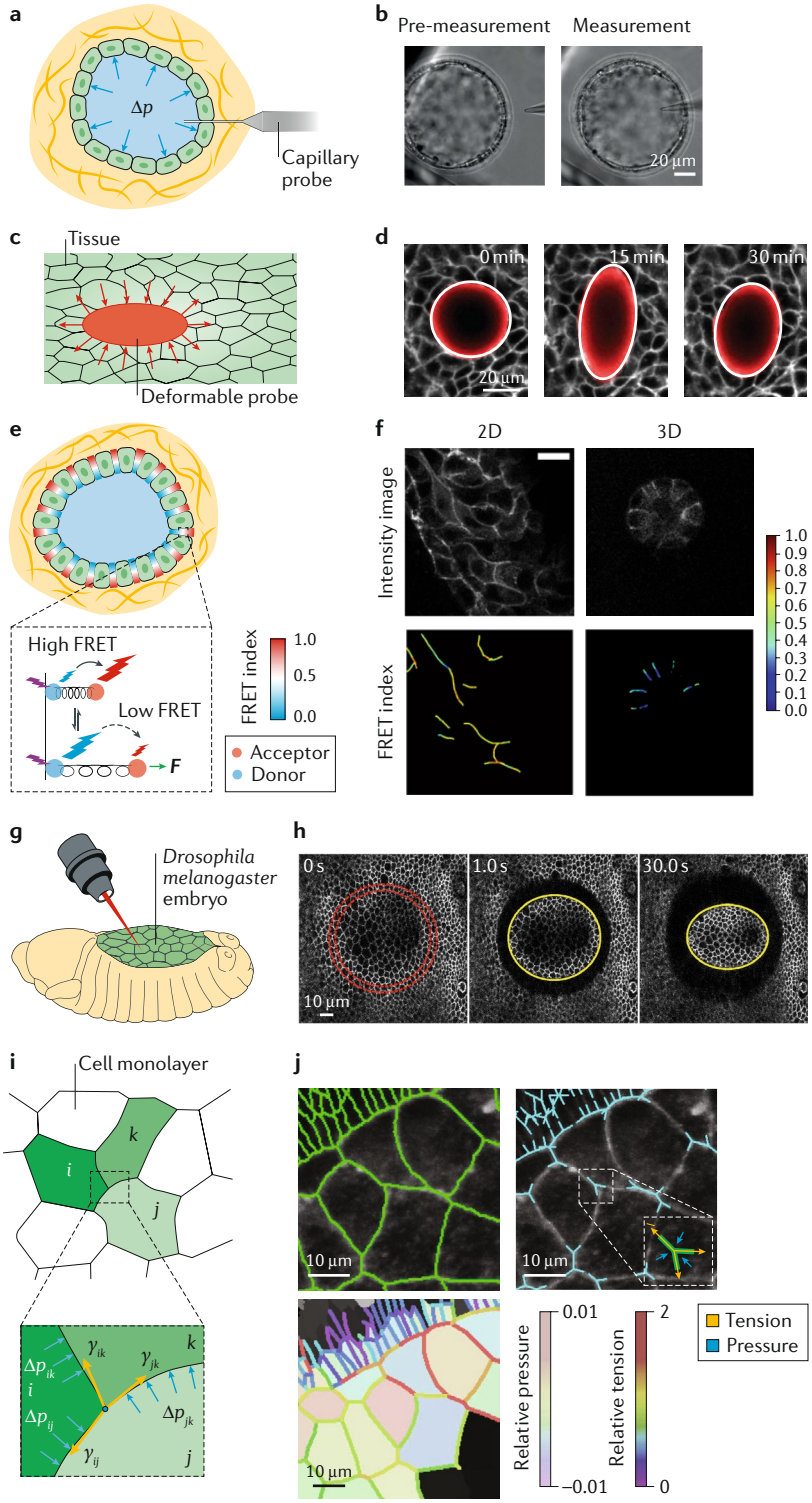

Fig. 3 | **Techniques for measuring internal stresses in vivo.** **a** | The servo-null method involves measuring the luminal pressure (Δp) of a tissue embedded in an elastic matrix by inserting a capillary probe directly into the lumen of the tissue. **b** | The servo-null method used to measure luminal pressure in a mouse blastocyst before (left) and during (right) measurement[140]. **c** | Inclusions (inert deformable probes) can be inserted into a tissue specimen to assess the local stress state. **d** | Application of inclusions (a liquid drop) as force transducers inserted into a tissue, before (0 min; left), 15 min (centre) and 30 min (right) after deformation[205]. **e** | Förster resonance energy transfer (FRET) tension sensors are genetically encoded molecular springs between two resonant fluorophores. Deformation of the molecular spring is reported as a change in FRET between the resonant fluorophores. **f** | Junctional tension reported by FRET sensors in an epithelial monolayer in 2D (left) and in an epithelial acinus in 3D (right)[168]. The scalebar represents the FRET index. **g** | In the laser-ablation technique, a specimen, such as a *Drosophila melanogaster* embryo, is cut using a pulsed laser and the internal stress is released. **h** | Circular laser cut (0 s; left) of a *D. melanogaster* embryo and asymmetrical retraction of the cut patch after 1 s (centre) and 30 s (right), owing to the differential internal tension along the *x* and *y* axes[173]. **i** | With force-inference methods, cellular pressures and intercellular tensions can be inferred from the changes in the geometry of the tissue. **j** | Illustration of a force-inference method. Cell monolayer segmentation (top left), tension and pressure location (top right) and calculated values for the cellular pressure and cell–cell junction tension (bottom left)[33,195]. Images part **b** reprinted from REF.[140], Springer Nature Limited. Images part **d** reprinted from REF.[205], Springer Nature Limited. Images part **f** reprinted with permission from REF.[168], Elsevier. Images part **h** reprinted with permission from REF.[173], The Royal Society. Images part **j** reprinted from REF.[33], Springer Nature Limited and with permission from REF.[195], Elsevier.

explain how epithelia actively maintain their integrity in many important physiological processes, such as swelling and 'hatching' (that is, emergence) of mammalian blastocysts from the zona pellucida[37,124,125].

The main advantage of the microbulge test is the robustness of the stress measurement, which is based only on mechanical equilibrium and, thus, there is no need to assume any constitutive behaviour for the epithelia. The main drawback of the technique is that it can only be applied to cell types that spontaneously form domes, unless transepithelial pressure is externally controlled.

Techniques for measuring stress in vivo

Techniques available to measure tractions and stresses in vivo include servo-null methods, inclusions, FRET tension stressors, laser ablation and force inference (TABLE 1).

Servo-null methods

The development of closed cavities with a pressurized, fluid-filled lumen is crucial for morphogenesis at different scales, ranging from tissues to organs[126]. The hydrostatic pressure in such cavities can be measured by directly puncturing the lumen with a micropipette connected to a micropressure-measuring system (FIG. 3a,b). Although quantitative measurement of pressure in animals dates back to the eighteenth century[127], the measurement of luminal pressure in micrometre-sized tissue structures was only achieved recently, thanks to the development of servo-null devices in the 1960s (REF.[128]). These devices use a glass micropipette filled with a saline solution electrolyte of very low electrical impedance, much lower than that of the luminal contents under study. When a fluid-filled pressurized cavity is punctured with the tip, the luminal contents are

pushed inside the tip, effectively increasing the electrical impedance measured at the micropipette. A servo-mechanism is then used to read the impedance at the tip and send a signal to a pressure transducer that will push the electrolyte towards the lumen until the original impedance is restored. The counterpressure applied by the transducer is assumed to be the pressure of the luminal cavity[129].

Although servo-null methods were originally developed to measure the pressure in the microcirculation[128,130], they have been used extensively in diverse systems and at different length scales, from the cytoplasm of a single cell[131,132] to whole animal organs[133–136]. Servo-null methods are also powerful tools for quantifying pressure in tissues, such as their early use to characterize pressurized domes formed by in vitro-grown epithelia[121], a tissue system in which luminal pressure is key for correct 3D morphogenesis. These methods have also been used to assess the key role of luminal pressure during heart development in zebrafish[137] and chicken[138] embryos and for quantifying the luminal pressure required for normal brain formation in chicken embryos[139]. More recently, these methods have been used to show that luminal pressure regulates cell-fate specification and tissue patterning during mouse blastocyst formation by influencing cell division and positioning[140], and to study the mechanoregulation of tissue morphogenesis by hydraulic feedback in the developing inner ear of zebrafish[141].

Despite their unique potential to measure pressure at the microscopic scale, servo-null methods have several disadvantages. For example, the tip resistance and compliance are usually neglected, overlooking a possible quantitative bias in the pressure measurements. From an experimental perspective, the filling of the tip needs to be meticulous and must be carefully assessed at all times, as even small bubbles will highly impact the measurement. Furthermore, micropipettes are prone to clogging during puncturing, thereby affecting pressure readings. Finally, the probing tips must be exceptionally thin to avoid leakage at the puncture site. Consequently, servo-null methods are highly complex and prone to very subtle but potentially catastrophic errors, in both the data collection and interpretation[142].

Inclusions as force transducers

A novel approach to measuring tissue stress in vivo and in vitro is based on introducing force transducers into a tissue and obtaining an optical readout (that is, a change in shape), typically using confocal microscopy (FIG. 3c,d). The probes used in these techniques must have a controlled size and shape and known visco-poroelastic properties, and their mechanical properties must be stable over time. For this reason, cells themselves cannot be used as force transducers, and these techniques resort to synthetic inclusions[39].

The first reported application of exogenous inserts as force transducers used fluorescently labelled liquid microdroplets of biocompatible fluorocarbon oils coated with adhesion molecules[143]. These microdroplets are injected into a tissue and their 3D shape is imaged using confocal microscopy. By knowing the surface tension of the microdroplet and assuming a spherical reference configuration, part of the deviatoric stress (BOX 2) locally applied on the surface of the microdroplet can be calculated. A crucial assumption of this method is that the surface tension of the microdroplets is constant and uniform. As the surface tension is altered when proteins are adsorbed on the microdroplet surface, the microdroplet must be saturated with surfactants prior to injection[32]. A fundamental limitation of microdroplet assays is the use of incompressible liquids, which impairs the measurement of the hydrostatic-stress component and the full-deviatoric-stress component (BOX 2), which has been overcome by using elastic reporters, such as hydrogel particles[144]. Furthermore, the use of exotic liquids, such as ferromagnetic fluids, enables the active application of forces on the surrounding tissue to provide a measurement of its mechanical properties and to study its active response to a mechanical stimulus[145].

A similar approach uses poroelastic polyacrylamide hydrogel microbeads rather than oil droplets[146,147]. Owing to their poroelastic nature, these microbeads are able to report on the hydrostatic-stress component (that is, the pressure). When the microbeads are subjected to a hydrostatic stress, their polymer-volume fraction changes and, consequently, the diffusion time of a small fluorescent tracer varies. By measuring this diffusion time, the hydrostatic component of the stress applied on the microbeads can be calculated. A more advanced approach uses alginate-hydrogel microbeads with fluorescent nanobeads embedded within them[148]. A fast iterative digital volume correlation algorithm[149] applied to microbead images enables the calculation of the full deformation configuration of each microbead. The full stress state on the microbead surface is then calculated from the deformation by using the FEM.

Lanthanide-doped nanoparticles are novel, promising transducers for force measurement in vivo[150,151], as they change their molecular structure when subjected to a mechanical stress, effectively varying their fluorescence-emission intensity[152]. These nanoparticles can be used as force reporters in the nano-Newton to micro-Newton regime[153], and, although used extensively as bioprobes[150], they remain to be used as force transducers in biological applications. Whispering-gallery-mode microlasers are another promising force transducer. They are micrometre-sized, deformable, optical microresonators that emit laser-light pulses with a frequency dependent on their geometry[154], thus, enabling quantification of their deformation from their emission spectrum. These reporters have been inserted into the cytoplasm of contractile cardiomyocytes and in zebrafish hearts to monitor cell and organ contractility, respectively[155], but they have yet to be used as direct force reporters.

Oil-microdroplet force transducers have been employed to study the stresses exerted by tooth mesenchymal cells in mandible explants ex vivo[143] and in 3D multicellular spheroids in vitro[156]. Conversely, elastic-hydrogel force transducers have been used to measure the hydrostatic stress in 3D multicellular spheroids[146,147]. Maps of the complete stress tensor have been obtained both in 3D tumour spheroids in vitro and in

zebrafish embryos in vivo by using viscoelastic-hydrogel force transducers[148].

The main advantage of force transducers is their ability to report the 3D internal stresses both in vitro and in vivo[143]. Owing to their small size and mechanical and chemical properties, they can be injected into embryos without compromising viability. However, limitations of microdroplets as force transducers include the need to know the surface tension of the microdroplet (and the assumption that it does not change after the microdroplet is injected into the sample) and that only some components of the stress tensor can be measured, both of which can be overcome by using hydrogel reporters[144,146–148,157]. Additional potential limitations include that the introduction of an exogenous body into the tissue might impact the measured stress distribution and affect tissue biochemical interactions, for example, by serving as a potential sink for lipophilic growth factors or by altering diffusion patterns in the tissue.

FRET tension sensors

FRET tension sensors consist of a molecular spring (that is, a short peptide) of known elastic constant and a fluorescence complex that reports elongation of the spring[158,159] (FIG. 3e,f). Sensors can be either encoded genetically or synthesized and coupled to an inert material. Different molecular springs have been designed, such as stFRET[160], TSMod[161] and sstFRET[162], and their elastic properties and force range have been characterized in vitro[160,161]. The elongation-reporter system comprises two fluorophores, a donor and an acceptor, with different but overlapping excitation and emission spectra[151]. The rate of energy transfer between the two fluorophores, first described by Theodore Förster[163], has the form:

$$K_{\mathrm{FRET}} \sim \frac{\kappa^2 J k_f}{n^4 r^6} \tag{8}$$

where κ is the relative dipolar orientation between the donor and acceptor, J is the integral of the overlap between the donor-emission and acceptor-excitation spectra, k_f is the radiative emission rate of the donor, n is the refraction index of the medium and r is the distance between the donor and the acceptor[151]. Because the rate of energy transfer depends on the separation between fluorophores, it can be converted into a tension readout after careful calibration.

FRET tension sensors have been extensively applied to the study of force transmission at focal adhesions in single cells[161]. At the multicellular level, they have been used to study intercellular tension in endothelial cell monolayers subjected to fluid shear[164], to elucidate the mechanical role of E-cadherin during collective cell migration in the *D. melanogaster* ovary[165] and to characterize the tension sustained by E-cadherin and desmosomes[166] during cell stretch[167] and swelling of epithelial acini[168], among other applications.

FRET tension sensors have the advantage that they can be genetically encoded and, therefore, can be expressed in virtually any living tissue, both in vitro and in vivo. Furthermore, they have the potential to report the forces sustained by different cellular components, are non-invasive and can be used with a fairly high throughput. However, despite the enormous potential of this technique, several limitations exist that restrict the range of applications for which it is suitable and question the interpretation of results[169]. It is typically assumed that FRET sensors are surrounded by a medium with the same refraction index as water, but local ion-concentration changes might greatly impact FRET measurements[151,170]. Furthermore, it is assumed that the FRET-sensor emission is affected only by the applied tension, but local chemical interactions of the FRET tension sensor with the microenvironment might impact its spring constant or introduce hysteresis[31,32]. The readout of FRET sensors is affected by fluorophore stability and readout quality is severely decreased in thick samples, in which the signal-to-noise ratio is reduced[31,151]. In addition, FRET sensors measure tension but not compression[31] and only provide the magnitude but not the direction of the tension[32]. Finally, besides these technical considerations, it is worth emphasizing that molecular tension does not necessarily reflect tissue stress, as tissue stress is supported by many different proteins arranged in parallel, and the tensional state of one such protein does not necessarily reflect the stress of the tissue.

Laser ablation

Laser ablation is used to assess the stress state of cohesive tissues and is based on simultaneously severing a group of cells to generate a sudden force imbalance. The movement of cells surrounding the ablated area to recover mechanical equilibrium is then used to compute relative values of stress before ablation[171,172] (FIG. 3g,h). The ablation is performed with near-infrared femtosecond lasers or pulsed ultraviolet lasers. Strain and stress anisotropy can be quantified by ablating a supracellular annular region of the tissue[173] or by severing circular areas[174].

The main assumptions underlying this technique are that the tissue is at mechanical equilibrium before and after the cut, that the ablation is able to release tissue tension and that dissipative forces outweigh inertia during relaxation[173,175]. By further assuming that dissipation is due to tissue viscosity and friction, the initial recoil velocity and its spatial profile provide information about the stress-to-viscosity and the friction-to-viscosity ratios[173]. However, given the complex rheological nature of tissues, it might not be accurate to assume a pure viscous response or uniform frictional properties, and, therefore, data from laser-ablation experiments should be combined with an appropriate analysis of tissue rheology[176,177]. The combination of non-uniform or anisotropic rheological descriptions with finite element models can provide more accurate interpretations of laser-ablation experiments[177].

Laser ablation has been extensively used to study early morphogenesis and wound healing. For example, laser ablation was used to show that dorsal closure in the *D. melanogaster* embryo is mechanically governed by the contractile forces exerted by purse strings at the leading edge of the lateral epidermis and by the actomyosin cortex of amnioserosa cells[175,178]. By ablating one amnioserosa cell, researchers showed that dorsal closure

by pulsed apical actomyosin constrictions that pull on the epidermis[179] is favoured. Ion flux between cells has also been related to the generation of contractile forces, measured with laser ablation during dorsal closure[180]. In *D. melanogaster* embryonic tissue, laser-ablation experiments showed that a contractile actomyosin cable forms along the wound margin, acting as a purse string[181]. In the zebrafish embryo, tissue tension has been related to the orientation of the mitotic spindle by measuring and manipulating the stress state using laser ablation[182].

The main advantages of laser ablation are that it can be used in vivo and in a wide range of tissues, and that it is fairly easy to implement with most optical-microscopy set-ups. However, major drawbacks of laser ablation include only providing relative stress measurements (unless a tissue rheology is assumed) and severe sample damage when a measurement is taken, thereby precluding time-lapse recordings. Finally, current laser-ablation implementations and analysis are largely restricted to a single optical plane, which prevents a full study of curved tissues.

Force-inference methods

Geometric force-inference methods compute the internal force balance of a tissue from images of the cellular contours (FIG. 3i,j). Internal forces include surface tensions (arising from the cortical cytoskeleton, adhesion proteins and/or the plasma membrane), internal pressures and the elastic and viscous response of cellular components[33]. By neglecting inertial forces, viscous dissipation and elastic contributions (assuming long timescales), only two sources of force are generally considered, namely, cellular surface tensions and internal pressure. Force-inference methods assume that tensions and pressures equilibrate at the vertices of the junctional network and at cell–cell interfaces, where Laplace's law, relating surface tension, pressure difference and curvature, is invoked (Eq. 7). With the assumptions mentioned above, relative tensions and pressures can be calculated without the need for a specific constitutive model of the system. Therefore, the tensions and pressure differences calculated with inference methods are determined up to a scaling constant factor, which can be obtained using an independent technique, such as micropipette aspiration[183,184] or TFM[185].

The assumptions underlying force-inference methods for epithelial tissues can be formalized using vertex models[186,187] (BOX 5). In a vertex model, the arrangement of cells in the tissue is described by a set of vertices that define the intersection of three or more cells. The mechanical state of the monolayer can be described by a work function, W, accounting for the work performed by cellular pressure and by surface tensions as the configuration of the tissue is perturbed. The out-of-balance forces at each vertex in the model can then be computed as:

$$\boldsymbol{f}^{v} = -\frac{\delta W}{\delta \boldsymbol{x}^{v}}, \tag{9}$$

where $\boldsymbol{f}^{v}$ represents the total force acting on vertex v, δW is the variation of work function and δx^{v} denotes the variation of the position of vertex v along the coordinate x^{v} (BOX 5). Mechanical equilibrium requires that $\boldsymbol{f}^{v} = \mathbf{0}$, providing one equation per vertex, which linearly depends on the unknown pressure and tension of adjacent cells. Thus, it is possible to establish an algebraic system of equations for cell pressure and surface tension just from the geometrical information of the epithelium[188]. However, by imposing force balance at the vertices where multiple cells meet, this system of equations is underdetermined[189]. Different approaches have been used to make the problem overdetermined, so the force-balance equation can be solved in the least-squares sense. One option is to assume uniform tension thereby reducing the unknowns to only the cell pressures[190]. This simplification is exact for foams and has been applied to model-specific tissues, such as the ommatidia of the *D. melanogaster* retina[191]. Alternatively, it can be assumed that every cell has the same pressure, keeping only the tensions as unknowns in the force-equilibrium equation[192]. In a different approach, by observing that most of the cell interfaces in epithelia are under positive tension, Bayesian statistics have been applied to reduce the number of unknowns while calculating both internal pressures and cortical tensions[189].

Recently, force inference has been combined with 2D TFM to study motile confluent epithelia, in an experimental set-up similar to MSM[185]. By knowing the tractions applied by the epithelial tissue, this approach enables the calculation of both the absolute tissue tensions and pressures, as well as the rheology of the monolayer.

All of the methods discussed above model the cell edges as straight lines between vertices, a geometry that is not always seen in epithelia. By relaxing the straight-cell-interface assumption, the force-balance equations become overdetermined[193]. This method, called CellFIT-2D[193] or Laplace inference[194], demands a much higher accuracy of image-segmentation algorithms to detect the curvature of cell boundaries[195]. Furthermore, the curvature of a cell–cell boundary in a 2D image will be smaller in general than that of the actual 3D surface. Laplace inference is well suited for tissues with high cell-edge curvature that is uniform along each cell boundary. However, for small or non-uniform curvatures along a cell edge, it is prone to artefacts and errors that propagate to neighbouring cells and have been shown to increase with increasing tissue size[194].

The problem of geometric force inference in 3D has been addressed in an extension of CellFIT-2D called CellFIT-3D[196]. The geometry of the sample is detected by segmentation of 3D image stacks obtained by confocal microscopy. Owing to the complexity of accurately segmenting fluorescent 3D images of cells and the subsequent extraction of surface curvatures, CellFIT-3D is only used to calculate cell tensions, while a natural theoretical extension to calculate pressures has been suggested[196].

In experimental set-ups in which slow motions cannot be assumed, the introduction of viscosity in the force-balance equation is required. In these cases, vertex models have been used to calculate the viscosity component of the internal forces of a cell monolayer[197,198]. In an approach called cinemechanometry[187] or video force

microscopy[199], cell pressures and tensions have been computed from the time evolution of the monolayer shape.

Geometric force-inference methods have been successfully applied in vivo to study the mechanics of development in *D. melanogaster*[199,200] and *Caenorhabditis elegans*[201]. They have also been pivotal to understanding the role of cell shape and mechanical stress orientation in mitosis in ex vivo models of *Xenopus laevis* embryonic tissue[202]. Among other contributions, force-inference methods have also been used to study the process of hair-cell determination in the avian cochlea[192] and the effect of interstitial fluid osmolarity in the tissue surface tension in progenitor cell segmentation during zebrafish gastrulation in vivo[203].

Force-inference methods have many advantages[32]: they are non-destructive, only requiring imaging of the tissue, they make minimal assumptions about the origin of the forces, they are well suited to be combined with other methods, such as suspended monolayers, and they provide cellular and tissue resolution. The limitations of these methods are that tensions along each cell edge are assumed to be positive and constant, which might not be true for wiggly junctions[194]; only ratios of tensions and pressure differences are calculated unless other techniques, such as micropipette aspiration, are used to provide absolute measurements of tensions[183,184]; accurate segmentation of the cell contour in the tissue is required; and the force calculation is currently limited to tractions transmitted between cells by contact, disregarding any force exerted by the cells on the substrate.

The assumptions underlying force-inference methods can be systematically tested in various ways, including geometrical inspection of the junctional network (wiggly junctions or non-uniform curvature being signs of non-compliance), a posteriori quantification of the error in the force-balance equations $\boldsymbol{f}^{v} = \mathbf{0}$ or comparisons with measurements relying on other techniques, such as servo-null pressure measurements, extended micropipette aspiration or laser-ablation tension measurements[194]. Furthermore, observation of cellular processes with mechanical consequences that are not accounted for in the conceptual framework underlying force inference, such as protrusive behaviour, cortex polarization or the presence of actin belts, may require reconsideration of the results or refinements of the underlying model.

Conclusions and outlook

A large, diverse suite of techniques is now available for researchers to measure stress with subcellular resolution in living tissues (summarized in TABLE 1). Although these techniques are still experimentally and computationally challenging, they are becoming more widely used, owing to the increased availability of open-source software[47] and standardized protocols. No technique is a one-size-fits-all solution, and a number of considerations must be taken into account before deciding which technique is more suitable for addressing a specific question. The highest spatial resolution is provided by tools to measure stress in 2D cultured monolayers, but these flat monolayers do not capture essential features of tissues in vivo. Conversely, whereas data generated with in vivo technologies might have greater physiological relevance, these methods generally do not provide absolute values of stress. The techniques reviewed here are not only relevant to illuminate biological processes in development, homeostasis and disease but are also important to advance our understanding of

Box 5 | **Vertex models**

The figure is an illustrative representation of the parameters and variables of a vertex model, including vertex v, edge λ, face κ, cell α, edge length l^{λ}, face area A^{κ}, cell volume V^{α}, vertex applied force $\boldsymbol{f}_{i}^{v}$, edge tension Λ^{λ}, surface tension T^{κ} and cell pressure p^{α}.

A vertex model describes the geometry of a tissue as a set of vertices marking the confluence of three or more cells (that is, triple junctions). The mechanical description of vertex models can be formulated by means of the work function, with an internal and an external component:

$$\delta W = \delta W_{i} + \delta W_{e}. \tag{23}$$

The external work differential accounts for any external force applied on the vertices:

$$\delta W_{e} = -\sum_{\text{vertex } v} \boldsymbol{f}_{e}^{v} \delta \boldsymbol{x}^{v}. \tag{24}$$

The internal work differential can be generally written as:

$$\delta W_{i} = \sum_{\text{cell } \alpha} -p^{\alpha}\delta V^{\alpha} + \sum_{\text{surface } \kappa} T^{\kappa}\delta A^{\kappa} + \sum_{\text{edge } \lambda} \Lambda^{\lambda}\delta l^{\lambda} - \sum_{\text{vertex } v} \boldsymbol{f}_{i}^{v}\delta \boldsymbol{x}^{v}, \tag{25}$$

where α labels each cell, κ and λ label each cell surface and edge, respectively, and v labels each vertex. δV^{α}, δA^{κ}, δl^{λ} and δx^{v} represent variations in cell volume, surface area, edge length and vertex position, respectively, while p^{α}, T^{κ}, Λ^{λ} and $\boldsymbol{f}_{i}^{v}$ indicate each cell's intracellular pressure, surface and line tensions, and internal dissipative forces applied on each vertex, respectively. A particular dissipative process is the internal viscosity of the epithelium, which can be modelled as:

$$f_{i,l}^{v} = \sum_{\text{vertex } v',j} \alpha_{lj}^{vv'} \frac{\mathrm{d}x_{j}^{v'}}{\mathrm{d}t}, \tag{26}$$

where j and l represent spatial coordinates. The equations describing the system are simplified for 2D flat monolayers, where the cells are assumed to be columnar and to have a uniform height. Thus, in Eq. 25, the cell area takes the role of the cell volume and the cell interfaces are treated as line edges with uniform line tension. Other energy functionals alternative to those in Eq. 25 have been proposed in the literature[206], with similar results.

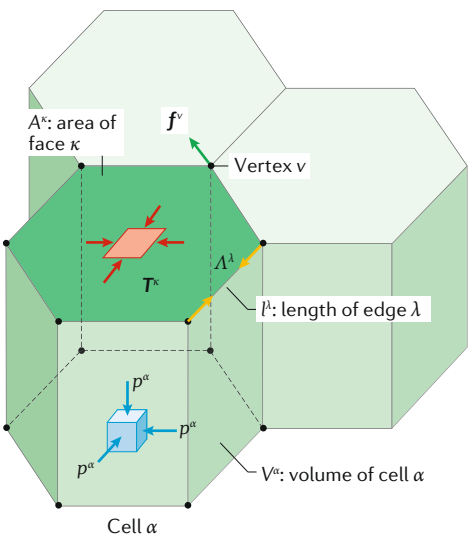

active-matter physics. In this context, measuring stress in reductionist tissues, such as micropatterned monolayers or even unidimensional multicellular chains, is the pertinent strategy to address questions such as what are the master equations that govern the dynamics of aggregates of active particles. A general problem of the techniques reviewed here is that they are still limited to a fairly low throughput. Overcoming this limitation is crucial to bring mechanobiology from the basic-science arena to applications in industry and medicine.

Published online 28 May 2020

1. Guillot, C. & Lecuit, T. Mechanics of epithelial tissue homeostasis and morphogenesis. *Science* **340**, 1185–1189 (2013).
2. Barker, N. Adult intestinal stem cells: critical drivers of epithelial homeostasis and regeneration. *Nat. Rev. Mol. Cell Biol.* **15**, 19–33 (2014).
3. Krndija, D. et al. Active cell migration is critical for steady-state epithelial turnover in the gut. *Science* **365**, 705–710 (2019).
4. Bruguês, A. et al. Forces driving epithelial wound healing. *Nat. Phys.* **10**, 683–690 (2014).
5. Northey, J. J., Przybyla, L. & Weaver, V. M. Tissue force programs cell fate and tumor aggression. *Cancer Discov.* **7**, 1224–1237 (2017).
6. Nia, H. T. et al. Solid stress and elastic energy as measures of tumour mechanopathology. *Nat. Biomed. Eng.* **1**, 0004 (2016).
7. Hannezo, E. & Heisenberg, C.-P. Mechanochemical feedback loops in development and disease. *Cell* **178**, 12–25 (2019).
8. Gudipaty, S. A. et al. Mechanical stretch triggers rapid epithelial cell division through Piezo1. *Nature* **543**, 118–121 (2017).
9. Benham-Pyle, B. W., Sim, J. Y., Hart, K. C., Pruitt, B. L. & Nelson, W. J. Increasing β-catenin/Wnt3A activity levels drive mechanical strain-induced cell cycle progression through mitosis. *eLife* **5**, e19799 (2016).
10. Uroz, M. et al. Regulation of cell cycle progression by cell–cell and cell–matrix forces. *Nat. Cell Biol.* **20**, 646–654 (2018).
11. Crick, F. H. C. & Hughes, A. F. W. The physical properties of cytoplasm. *Exp. Cell Res.* **1**, 37–80 (1950).
12. Bausch, A. R., Möller, W. & Sackmann, E. Measurement of local viscoelasticity and forces in living cells by magnetic tweezers. *Biophys. J.* **76**, 573–579 (1999).
13. Ashkin, A. Acceleration and trapping of particles by radiation pressure. *Phys. Rev. Lett.* **24**, 156–159 (1970).
14. Ashkin, A., Dziedzic, J. M., Bjorkholm, J. E. & Chu, S. Observation of a single-beam gradient force optical trap for dielectric particles. *Opt. Lett.* **11**, 288–290 (1986).
15. Wu, J. Acoustical tweezers. *J. Acoust. Soc. Am.* **89**, 2140–2143 (1991).
16. Binnig, G., Quate, C. F. & Gerber, C. Atomic force microscope. *Phys. Rev. Lett.* **56**, 930–933 (1986).
17. Mitchison, J. M. & Swann, M. M. The mechanical properties of the cell surface: I. The cell elastimeter. *J. Exp. Biol.* **31**, 443–460 (1954).
18. Zamir, E. A., Srinivasan, V., Perucchio, R. & Taber, L. A. Mechanical asymmetry in the embryonic chick heart during looping. *Ann. Biomed. Eng.* **31**, 1327–1336 (2003).
19. Foty, R. A., Forgacs, G., Pfleger, C. M. & Steinberg, M. S. Liquid properties of embryonic tissues: measurement of interfacial tensions. *Phys. Rev. Lett.* **72**, 2298–2301 (1994).
20. Brillouin, L. Diffusion de la lumière et des rayons X par un corps transparent homogène. *Ann. Phys. (Paris)* **9**, 88–122 (1922).
21. Scarcelli, G. & Yun, S. H. Confocal Brillouin microscopy for three-dimensional mechanical imaging. *Nat. Photonics* **2**, 39–43 (2008).
22. Moore, A. R. & Burt, A. S. On the locus and nature of the forces causing gastrulation in the embryos of *Dendraster excentricus*. *J. Exp. Zool.* **82**, 159–171 (1939).
23. Rehfeldt, F. & Schmidt, C. F. Physical probing of cells. *J. Phys. D. Appl. Phys.* **50**, 463001 (2017).
24. Basoli, F. et al. Biomechanical characterization at the cell scale: present and prospects. *Front. Physiol.* **9**, 1449 (2018).
25. Zhang, H. & Liu, K.-K. Optical tweezers for single cells. *J. R. Soc. Interface* **5**, 671–690 (2008).
26. Favre-Bulle, I. A., Stilgoe, A. B., Scott, E. K. & Rubinsztein-Dunlop, H. Optical trapping in vivo: theory, practice, and applications. *Nanophotonics* **8**, 1023–1040 (2019).
27. Ozcelik, A. et al. Acoustic tweezers for the life sciences. *Nat. Methods* **15**, 1021–1028 (2018).
28. Krieg, M. et al. Atomic force microscopy-based mechanobiology. *Nat. Rev. Phys.* **1**, 41–57 (2019).
29. Hochmuth, R. M. Micropipette aspiration of living cells. *J. Biomech.* **33**, 15–22 (2000).
30. González-Bermúdez, B., Guinea, G. V. & Plaza, G. R. Advances in micropipette aspiration: applications in cell biomechanics, models, and extended studies. *Biophys. J.* **116**, 587–594 (2019).
31. Campàs, O. A toolbox to explore the mechanics of living embryonic tissues. *Semin. Cell Dev. Biol.* **55**, 119–130 (2016).
32. Sugimura, K., Lenne, P.-F. & Graner, F. Measuring forces and stresses in situ in living tissues. *Development* **143**, 186–196 (2016).
33. Roca-Cusachs, P., Conte, V. & Trepat, X. Quantifying forces in cell biology. *Nat. Cell Biol.* **19**, 742–751 (2017).
34. Prevedel, R., Diz-Muñoz, A., Ruocco, G. & Antonacci, G. Brillouin microscopy: an emerging tool for mechanobiology. *Nat. Methods* **16**, 969–977 (2019).
35. Pérez-González, C. et al. Active wetting of epithelial tissues. *Nat. Phys.* **15**, 79–88 (2019).
36. Bergert, M. et al. Confocal reference free traction force microscopy. *Nat. Commun.* **7**, 12814 (2016).
37. Latorre, E. et al. Active superelasticity in three-dimensional epithelia of controlled shape. *Nature* **563**, 203–208 (2018).
This paper reports the first use of the microbulge test to measure the internal stress of a curved epithelium.
38. Ban, E. et al. Mechanisms of plastic deformation in collagen networks induced by cellular forces. *Biophys. J.* **114**, 450–461 (2018).
39. Girardo, S. et al. Standardized microgel beads as elastic cell mechanical probes. *J. Mater. Chem. B* **6**, 6245–6261 (2018).
40. Saw, T. B. et al. Topological defects in epithelia govern cell death and extrusion. *Nature* **544**, 212–216 (2017).
41. Wang, N. et al. Cell prestress. I. Stiffness and prestress are closely associated in adherent contractile cells. *Am. J. Physiol. Cell Physiol.* **282**, C606–C616 (2002).
Description of the general concept underlying MSM, applied here to the inference of internal stress in a single cell.
42. Harris, A. K., Wild, P. & Stopak, D. Silicone rubber substrata: a new wrinkle in the study of cell locomotion. *Science* **208**, 177–179 (1980).
First qualitative implementation of TFM, based on the observation that cells are able to wrinkle thin polymer substrates.
43. Lee, J., Leonard, M., Oliver, T., Ishihara, A. & Jacobson, K. Traction forces generated by locomoting keratocytes. *J. Cell Biol.* **127**, 1957–1964 (1994).
44. Oliver, T., Dembo, M. & Jacobson, K. Traction forces in locomoting cells. *Cell Motil. Cytoskeleton* **31**, 225–240 (1995).
45. Dembo, M., Oliver, T., Ishihara, A. & Jacobson, K. Imaging the traction stresses exerted by locomoting cells with the elastic substratum method. *Biophys. J.* **70**, 2008–2022 (1996).
46. Dembo, M. & Wang, Y.-L. Stresses at the cell-to-substrate interface during locomotion of fibroblasts. *Biophys. J.* **76**, 2307–2316 (1999).
This study reports the first quantitative implementation of 2D TFM.
47. Schwarz, U. S. & Soiné, J. R. D. Traction force microscopy on soft elastic substrates: A guide to recent computational advances. *Biochim. Biophys. Acta* **1853**, 3095–3104 (2015).
48. Style, R. W. et al. Traction force microscopy in physics and biology. *Soft Matter* **10**, 4047–4055 (2014).
49. Polio, S. R., Rothenberg, K. E., Stamenović, D. & Smith, M. L. A micropatterning and image processing approach to simplify measurement of cellular traction forces. *Acta Biomater.* **8**, 82–88 (2012).
50. Butler, J. P., Tolić-Nørrelykke, I. M., Fabry, B. & Fredberg, J. J. Traction fields, moments, and strain energy that cells exert on their surroundings. *Am. J. Physiol. Cell Physiol.* **282**, C595–C605 (2002).
This paper formulates Fourier 2D TFM, resulting in the speeding up of traction calculations by orders of magnitude.
51. del Álamo, J. C. et al. Spatio-temporal analysis of eukaryotic cell motility by improved force cytometry. *Proc. Natl Acad. Sci. USA* **104**, 13343–13348 (2007).
52. Schwarz, U. S. et al. Calculation of forces at focal adhesions from elastic substrate data: the effect of localized force and the need for regularization. *Biophys. J.* **83**, 1380–1394 (2002).
53. Sabass, B., Gardel, M. L., Waterman, C. M. & Schwarz, U. S. High resolution traction force microscopy based on experimental and computational advances. *Biophys. J.* **94**, 207–220 (2008).
54. Huang, Y. et al. Traction force microscopy with optimized regularization and automated Bayesian parameter selection for comparing cells. *Sci. Rep.* **9**, 539 (2019).
55. Yang, Z., Lin, J.-S., Chen, J. & Wang, J. H.-C. Determining substrate displacement and cell traction fields — a new approach. *J. Theor. Biol.* **242**, 607–616 (2006).
56. Griffin, B. P., Largaespada, C. J., Rinaldi, N. A. & Lemmon, C. A. A novel method for quantifying traction forces on hexagonal micropatterned protein features on deformable poly-dimethyl siloxane sheets. *MethodsX* **6**, 1343–1352 (2019).
57. Burton, K. & Taylor, D. L. Traction forces of cytokinesis measured with optically modified elastic substrata. *Nature* **385**, 450–454 (1997).
58. Elosegui-Artola, A. et al. Mechanical regulation of a molecular clutch defines force transmission and transduction in response to matrix rigidity. *Nat. Cell Biol.* **18**, 540–548 (2016).
59. Balaban, N. Q. et al. Force and focal adhesion assembly: a close relationship studied using elastic micropatterned substrates. *Nat. Cell Biol.* **3**, 466–472 (2001).
60. Trepat, X. et al. Physical forces during collective cell migration. *Nat. Phys.* **5**, 426–430 (2009).
61. Serra-Picamal, X. et al. Mechanical waves during tissue expansion. *Nat. Phys.* **8**, 628–634 (2012).
62. Sunyer, R. et al. Collective cell durotaxis emerges from long-range intercellular force transmission. *Science* **353**, 1157–1161 (2016).
63. Kim, J. H. et al. Propulsion and navigation within the advancing monolayer sheet. *Nat. Mater.* **12**, 856–863 (2013).
64. Park, J.-A. et al. Unjamming and cell shape in the asthmatic airway epithelium. *Nat. Mater.* **14**, 1040–1048 (2015).
65. Uroz, M. et al. Traction forces at the cytokinetic ring regulate cell division and polyploidy in the migrating zebrafish epicardium. *Nat. Mater.* **18**, 1015–1023 (2019).
66. Jerison, E. R., Xu, Y., Wilen, L. A. & Dufresne, E. R. Deformation of an elastic substrate by a three-phase contact line. *Phys. Rev. Lett.* **106**, 186103 (2011).
67. Xu, Y. et al. Imaging in-plane and normal stresses near an interface crack using traction force microscopy. *Proc. Natl Acad. Sci. USA* **107**, 14964–14967 (2010).
68. Casares, L. et al. Hydraulic fracture during epithelial stretching. *Nat. Mater.* **14**, 343–351 (2015).
69. Oria, R. et al. Force loading explains spatial sensing of ligands by cells. *Nature* **552**, 219–224 (2017).
70. Nguyen, D. T. et al. Surface pressure and shear stress fields within a frictional contact on rubber. *J. Adhes.* **87**, 235–250 (2011).
71. Chateauminois, A. & Fretigny, C. Local friction at a sliding interface between an elastomer and a rigid spherical probe. *Eur. Phys. J. E Soft Matter* **27**, 221–227 (2008).
72. del Álamo, J. C. et al. Three-dimensional quantification of cellular traction forces and mechanosensing of thin substrata by Fourier traction force microscopy. *PLoS ONE* **8**, e69850 (2013).
This paper formulates Fourier 2.5D TFM.

73. Álvarez-González, B. et al. Cytoskeletal mechanics regulating amoeboid cell locomotion. *Appl. Mech. Rev.* **66**, 050804 (2014).
74. Tan, J. L. et al. Cells lying on a bed of microneedles: an approach to isolate mechanical force. *Proc. Natl Acad. Sci. USA* **100**, 1484–1489 (2003).
This paper pioneered the use of micropillar arrays for force quantification.
75. Saez, A., Ghibaudo, M., Buguin, A., Silberzan, P. & Ladoux, B. Rigidity-driven growth and migration of epithelial cells on microstructured anisotropic substrates. *Proc. Natl Acad. Sci. USA* **104**, 8281–8286 (2007).
76. Legant, W. R. et al. Microfabricated tissue gauges to measure and manipulate forces from 3D microtissues. *Proc. Natl Acad. Sci. USA* **106**, 10097–10102 (2009).
77. Boudou, T. et al. A microfabricated platform to measure and manipulate the mechanics of engineered cardiac microtissues. *Tissue Eng. Part A* **18**, 910–919 (2012).
78. du Roure, O. et al. Force mapping in epithelial cell migration. *Proc. Natl Acad. Sci. USA* **102**, 2390–2395 (2005).
79. Rabodzey, A., Alcaide, P., Luscinskas, F. W. & Ladoux, B. Mechanical forces induced by the transendothelial migration of human neutrophils. *Biophys. J.* **95**, 1428–1438 (2008).
80. Reffay, M. et al. Interplay of RhoA and mechanical forces in collective cell migration driven by leader cells. *Nat. Cell Biol.* **16**, 217–223 (2014).
81. Saez, A. et al. Traction forces exerted by epithelial cell sheets. *J. Phys. Condens. Matter* **22**, 194119 (2010).
82. Yang, B. et al. Stopping transformed cancer cell growth by rigidity sensing. *Nat. Mater.* **19**, 239–250 (2020).
83. Schoen, I., Hu, W., Klotzsch, E. & Vogel, V. Probing cellular traction forces by micropillar arrays: contribution of substrate warping to pillar deflection. *Nano Lett.* **10**, 1823–1830 (2010).
84. Liu, Z. et al. Mechanical tugging force regulates the size of cell–cell junctions. *Proc. Natl Acad. Sci. USA* **107**, 9944–9949 (2010).
85. Bastounis, E., Álvarez-González, B., del Álamo, J. C., Lasheras, J. C. & Firtel, R. A. Cooperative cell motility during tandem locomotion of amoeboid cells. *Mol. Biol. Cell* **27**, 1262–1271 (2016).
86. Maruthamuthu, V., Sabass, B., Schwarz, U. S. & Gardel, M. L. Cell–ECM traction force modulates endogenous tension at cell–cell contacts. *Proc. Natl Acad. Sci. USA* **108**, 4708–4713 (2011).
87. Ng, M. R., Besser, A., Brugge, J. S. & Danuser, G. Mapping the dynamics of force transduction at cell–cell junctions of epithelial clusters. *eLife* **3**, e03282 (2014).
88. Tambe, D. T. et al. Monolayer stress microscopy: limitations, artifacts, and accuracy of recovered intercellular stresses. *PLoS ONE* **8**, e55172 (2013).
89. Tambe, D. T. et al. Collective cell guidance by cooperative intercellular forces. *Nat. Mater.* **10**, 469–475 (2011).
This paper marks the rigorous mathematical formulation of MSM to compute all components of the stress tensor in a cell monolayer.
90. Moussus, M. et al. Intracellular stresses in patterned cell assemblies. *Soft Matter* **10**, 2414–2423 (2014).
91. Nier, V. et al. Inference of internal stress in a cell monolayer. *Biophys. J.* **110**, 1625–1635 (2016).
92. Serrano, R. et al. Three-dimensional monolayer stress microscopy. *Biophys. J.* **117**, 111–128 (2019).
93. Timoshenko, S. & Woinowsky-Krieger, S. *Theory of Plates and Shells* 2nd edn (McGraw-Hill, 1959).
94. Vishwakarma, M. et al. Mechanical interactions among followers determine the emergence of leaders in migrating epithelial cell collectives. *Nat. Commun.* **9**, 3469 (2018).
95. Harris, A. R. et al. Characterizing the mechanics of cultured cell monolayers. *Proc. Natl Acad. Sci. USA* **109**, 16449–16454 (2012).
This paper shows the first implementation of the suspended-monolayer technique.
96. Khalilgharibi, N. et al. Stress relaxation in epithelial monolayers is controlled by the actomyosin cortex. *Nat. Phys.* **15**, 839–847 (2019).
97. Harris, A. R. et al. Generating suspended cell monolayers for mechanobiological studies. *Nat. Protoc.* **8**, 2516–2530 (2013).
98. Merzouki, A., Malaspinas, O. & Chopard, B. The mechanical properties of a cell-based numerical model of epithelium. *Soft Matter* **12**, 4745–4754 (2016).
99. Wyatt, T. P. J. et al. Emergence of homeostatic epithelial packing and stress dissipation through divisions oriented along the long cell axis. *Proc. Natl Acad. Sci. USA* **112**, 5726–5731 (2015).
100. Xu, G.-K., Liu, Y. & Zheng, Z. Oriented cell division affects the global stress and cell packing geometry of a monolayer under stretch. *J. Biomech.* **49**, 401–407 (2016).
101. Wyatt, T. P. J. et al. Actomyosin controls planarity and folding of epithelia in response to compression. *Nat. Mater.* **19**, 109–117 (2020).
102. Fouchard, J. et al. Curling of epithelial monolayers reveals coupling between active bending and tissue tension. *Proc. Natl Acad. Sci. USA* **117**, 9377–9383 (2020).
103. Bloom, R. J., George, J. P., Celedon, A., Sun, S. X. & Wirtz, D. Mapping local matrix remodeling induced by a migrating tumor cell using three-dimensional multiple-particle tracking. *Biophys. J.* **95**, 4077–4088 (2008).
104. Hur, S. S., Zhao, Y., Li, Y.-S., Botvinick, E. & Chien, S. Live cells exert 3-dimensional traction forces on their substrata. *Cell Mol. Bioeng.* **2**, 425–436 (2009).
105. Álvarez-González, B. et al. Three-dimensional balance of cortical tension and axial contractility enables fast amoeboid migration. *Biophys. J.* **108**, 821–832 (2015).
106. Maskarinec, S. A., Franck, C., Tirrell, D. A. & Ravichandran, G. Quantifying cellular traction forces in three dimensions. *Proc. Natl Acad. Sci. USA* **106**, 22108–22113 (2009).
107. Toyjanova, J. et al. High resolution, large deformation 3D traction force microscopy. *PLoS ONE* **9**, e90976 (2014).
108. Delanoë-Ayari, H., Rieu, J. P. & Sano, M. 4D traction force microscopy reveals asymmetric cortical forces in migrating *Dictyostelium* cells. *Phys. Rev. Lett.* **105**, 248103 (2010).
109. Aung, A. et al. 3D traction stresses activate protease-dependent invasion of cancer cells. *Biophys. J.* **107**, 2528–2537 (2014).
110. Yeh, Y.-T. et al. Three-dimensional forces exerted by leukocytes and vascular endothelial cells dynamically facilitate diapedesis. *Proc. Natl Acad. Sci. USA* **115**, 133–138 (2018).
111. Álvarez-González, B. et al. Two-layer elastographic 3-D traction force microscopy. *Sci. Rep.* **7**, 39315 (2017).
112. Gordon, V. D. et al. Measuring the mechanical stress induced by an expanding multicellular tumor system: a case study. *Exp. Cell Res.* **289**, 58–66 (2003).
This paper reports a pioneering implementation of 3D TFM.
113. Zhou, J., Pal, S., Maiti, S. & Davidson, L. A. Force production and mechanical accommodation during convergent extension. *Development* **142**, 692–701 (2015).
114. Legant, W. R. et al. Measurement of mechanical tractions exerted by cells in three-dimensional matrices. *Nat. Methods* **7**, 969–971 (2010).
115. Steinwachs, J. et al. Three-dimensional force microscopy of cells in biopolymer networks. *Nat. Methods* **13**, 171–176 (2016).
116. Mark, C. et al. Collective forces of tumor spheroids in three-dimensional biopolymer networks. *eLife* **9**, e51912 (2020).
117. Alessandri, K. et al. Cellular capsules as a tool for multicellular spheroid production and for investigating the mechanics of tumor progression in vitro. *Proc. Natl Acad. Sci. USA* **110**, 14843–14848 (2013).
118. Leonavicius, K. et al. Mechanics of mouse blastocyst hatching revealed by a hydrogel-based microdeformation assay. *Proc. Natl Acad. Sci. USA* **115**, 10375–10380 (2018).
119. Leighton, J., Brada, Z., Estes, L. W. & Justh, G. Secretory activity and oncogenicity of a cell line (MDCK) derived from canine kidney. *Science* **163**, 472–473 (1969).
120. Rabito, C. A., Tchao, R., Valentich, J. & Leighton, J. Effect of cell–substratum interaction on hemicyst formation by MDCK cells. *In Vitro* **16**, 461–468 (1980).
121. Tanner, C., Frambach, D. A. & Misfeldt, D. S. Transepithelial transport in cell culture. A theoretical and experimental analysis of the biophysical properties of domes. *Biophys. J.* **43**, 183–190 (1983).
This paper reports the first application of a servo-null device to an in vitro-grown tissue.
122. de Laplace, P.- S. *Supplément au dixième livre du Traité de Mécanique Céleste: Sur L'Action Capillaire* Vol. 4 (Chez J. B. M. Duprat, 1805).
123. Lamb, H. *Statics: Including Hydrostatics and the Elements of the Theory of Elasticity* 3rd edn (Cambridge Univ. Press, 1960).
124. Hildebrand, S. et al. The E-cadherin/AmotL2 complex organizes actin filaments required for epithelial hexagonal packing and blastocyst hatching. *Sci. Rep.* **7**, 9540 (2017).
125. Deglincerti, A. et al. Self-organization of the in vitro attached human embryo. *Nature* **533**, 251–254 (2016).
126. Navis, A. & Bagnat, M. Developing pressures: fluid forces driving morphogenesis. *Curr. Opin. Genet. Dev.* **32**, 24–30 (2015).
127. Hales, S. *Statical Essays, Containing Haemastaticks, or, An Account of Some Hydraulick and Hydrostatical Experiments Made on the Blood and Blood Vessels of Animals* (W. Innys and R. Manby, 1733).
128. Wiederhielm, C. A., Woodbury, J. W., Kirk, S. & Rushmer, R. F. Pulsatile pressures in the microcirculation of frog's mesentery. *Am. J. Physiol.* **207**, 173–176 (1964).
Implementation of servo-null systems and their application to measure pulsatile pressure in a capillary.
129. Petrie, R. J. & Koo, H. Direct measurement of intracellular pressure. *Curr. Protoc. Cell Biol.* **63**, 12.9.1–12.9.9 (2014).
130. Falchuk, K. H. & Berliner, R. W. Hydrostatic pressures in peritubular capillaries and tubules in the rat kidney. *Am. J. Physiol.* **220**, 1422–1426 (1971).
131. Kelly, S. M. & Macklem, P. T. Direct measurement of intracellular pressure. *Am. J. Physiol.* **260**, C652–C657 (1991).
132. Petrie, R. J., Koo, H. & Yamada, K. M. Generation of compartmentalized pressure by a nuclear piston governs cell motility in a 3D matrix. *Science* **345**, 1062–1065 (2014).
133. Myers, R. R., Rydevik, B. L., Heckman, H. M. & Powell, H. C. Proximodistal gradient in endoneurial fluid pressure. *Exp. Neurol.* **102**, 368–370 (1988).
134. Wit, H. P., Thalen, E. O. & Albers, F. W. J. Dynamics of inner ear pressure release, measured with a double-barreled micropipette in the guinea pig. *Hearing Res.* **132**, 131–139 (1999).
135. Avila, M. Y., Carré, D. A., Stone, R. A. & Civan, M. M. Reliable measurement of mouse intraocular pressure by a servo-null micropipette system. *Investig. Ophthalmol. Vis. Sci.* **42**, 1841–1846 (2001).
136. Hu, N., Yost, H. J. & Clark, E. B. Cardiac morphology and blood pressure in the adult zebrafish. *Anat. Rec.* **264**, 1–12 (2001).
137. Hu, N., Sedmera, D., Yost, H. J. & Clark, E. B. Structure and function of the developing zebrafish heart. *Anat. Rec.* **260**, 148–157 (2000).
138. Stekelenburg-de Vos, S. et al. Systolic and diastolic ventricular function assessed by pressure-volume loops in the stage 21 venous clipped chick embryo. *Pediatr. Res.* **57**, 16–21 (2005).
139. Desmond, M. E., Levitan, M. L. & Haas, A. R. Internal luminal pressure during early chick embryonic brain growth: descriptive and empirical observations. *Anat. Rec.* **285**, 737–747 (2005).
140. Chan, C. J. et al. Hydraulic control of mammalian embryo size and cell fate. *Nature* **571**, 112–116 (2019).
141. Mosaliganti, K. R. et al. Size control of the inner ear via hydraulic feedback. *eLife* **8**, e39596 (2019).
142. Lorenz, J. N. Micropuncture of the kidney: a primer on techniques. *Compr. Physiol.* **2**, 621–637 (2012).
143. Campàs, O. et al. Quantifying cell-generated mechanical forces within living embryonic tissues. *Nat. Methods* **11**, 183–189 (2014).
This paper reports the first use of exogenous inclusions as cell-force transducers.
144. Vorselen, D. et al. Microparticle traction force microscopy reveals subcellular force exertion patterns in immune cell–target interactions. *Nat. Commun.* **11**, 20 (2020).
145. Serwane, F. et al. In vivo quantification of spatially varying mechanical properties in developing tissues. *Nat. Methods* **14**, 181–186 (2017).
146. Ingremeau, F. et al. Optical sensing of mechanical pressure based on diffusion measurement in polyacrylamide cell-like barometers. *Soft Matter* **13**, 4210–4213 (2017).
147. Dolega, M. E. et al. Cell-like pressure sensors reveal increase of mechanical stress towards the core of multicellular spheroids under compression. *Nat. Commun.* **8**, 14056 (2017).
148. Mohagheghian, E. et al. Quantifying compressive forces between living cell layers and within tissues using elastic round microgels. *Nat. Commun.* **9**, 1878 (2018).
149. Bar-Kochba, E., Toyjanova, J., Andrews, E., Kim, K.-S. & Franck, C. A fast iterative digital volume correlation

algorithm for large deformations. *Exp. Mech.* **55**, 261–274 (2015).
150. Shen, J., Sun, L.-D. & Yan, C.-H. Luminescent rare earth nanomaterials for bioprobe applications. *Dalton Trans.* **42**, 5687–5697 (2008).
151. Mehlenbacher, R. D., Kolbl, R., Lay, A. & Dionne, J. A. Nanomaterials for *in vivo* imaging of mechanical forces and electrical fields. *Nat. Rev. Mater.* **3**, 17080 (2018).
152. Wisser, M. D. et al. Strain-induced modification of optical selection rules in lanthanide-based upconverting nanoparticles. *Nano Lett.* **15**, 1891–1897 (2015).
153. Lay, A. et al. Upconverting nanoparticles as optical sensors of nano- to micro-Newton forces. *Nano Lett.* **17**, 4172–4177 (2017).
154. Humar, M. & Yun, S. H. Intracellular microlasers. *Nat. Photonics* **9**, 572–576 (2015).
155. Schubert, M. et al. Monitoring contractility in single cardiomyocytes and whole hearts with bio-integrated microlasers. *Prepr. bioRxiv* https://doi.org/10.1101/605444 (2019).
156. Lucio, A. A. et al. Spatiotemporal variation of endogenous cell-generated stresses within 3D multicellular spheroids. *Sci. Rep.* **7**, 12022 (2017).
157. Träber, N. et al. Polyacrylamide bead sensors for *in vivo* quantification of cell-scale stress in zebrafish development. *Sci. Rep.* **9**, 17031 (2019).
158. Gayrard, C. & Borghi, N. FRET-based molecular tension microscopy. *Methods* **94**, 33–42 (2016).
159. Yasunaga, A., Murad, Y. & Li, I. T. S. Quantifying molecular tension-classifications, interpretations and limitations of force sensors. *Phys. Biol.* **17**, 011001 (2019).
160. Meng, F., Suchyna, T. M. & Sachs, F. A fluorescence energy transfer-based mechanical stress sensor for specific proteins *in situ*. *FEBS J.* **275**, 3072–3087 (2008).
161. Grashoff, C. et al. Measuring mechanical tension across vinculin reveals regulation of focal adhesion dynamics. *Nature* **466**, 263–266 (2010).
162. Meng, F. & Sachs, F. Visualizing dynamic cytoplasmic forces with a compliance-matched FRET sensor. *J. Cell Sci.* **124**, 261–269 (2011).
163. Förster, T. Zwischenmolekulare Energiewanderung und Fluoreszenz. *Ann. Phys. (Leipz.)* **437**, 55–75 (1948).
164. Conway, D. E. et al. Fluid shear stress on endothelial cells modulates mechanical tension across VE-cadherin and PECAM-1. *Curr. Biol.* **23**, 1024–1030 (2013).
165. Cai, D. et al. Mechanical feedback through E-cadherin promotes direction sensing during collective cell migration. *Cell* **157**, 1146–1159 (2014).
166. Price, A. J. et al. Mechanical loading of desmosomes depends on the magnitude and orientation of external stress. *Nat. Commun.* **9**, 5284 (2018).
167. Borghi, N. et al. E-cadherin is under constitutive actomyosin-generated tension that is increased at cell–cell contacts upon externally applied stretch. *Proc. Natl Acad. Sci. USA* **109**, 12568–12573 (2012).
168. Narayanan, V. et al. Osmotic gradients in epithelial acini increase mechanical tension across E-cadherin, drive morphogenesis, and maintain homeostasis. *Curr. Biol.* **30**, 624–633 (2020).
169. Eder, D., Basler, K. & Aegerter, C. M. Challenging FRET-based E-cadherin force measurements in *Drosophila*. *Sci. Rep.* **7**, 13692 (2017).
170. Stabley, D. R., Jurchenko, C., Marshall, S. S. & Salaita, K. S. Visualizing mechanical tension across membrane receptors with a fluorescent sensor. *Nat. Methods* **9**, 64–67 (2012).
171. Colombelli, J. & Solon, J. Force communication in multicellular tissues addressed by laser nanosurgery. *Cell Tissue Res.* **352**, 133–147 (2013).
172. Zulueta-Coarasa, T. & Fernandez-Gonzalez, R. in *Integrative Mechanobiology: Micro- and Nano-Techniques in Cell Mechanobiology* Ch. 8 (eds Sun, Y., Kim, D.-H. & Simmons, C. A.) 128–147 (Cambridge Univ. Press, 2015).
173. Bonnet, I. et al. Mechanical state, material properties and continuous description of an epithelial tissue. *J. R. Soc. Interface* **9**, 2614–2623 (2012).
174. Etournay, R. et al. Interplay of cell dynamics and epithelial tension during morphogenesis of the *Drosophila* pupal wing. *eLife* **4**, e07090 (2015).
175. Hutson, M. S. et al. Forces for morphogenesis investigated with laser microsurgery and quantitative modeling. *Science* **300**, 145–149 (2003).
176. Ma, X., Lynch, H. E., Scully, P. C. & Hutson, M. S. Probing embryonic tissue mechanics with laser hole drilling. *Phys. Biol.* **6**, 036004 (2009).
177. Hutson, M. S. et al. Combining laser microsurgery and finite element modeling to assess cell-level epithelial mechanics. *Biophys. J.* **97**, 3075–3085 (2009).
178. Kiehart, D. P., Galbraith, C. G., Edwards, K. A., Rickoll, W. L. & Montague, R. A. Multiple forces contribute to cell sheet morphogenesis for dorsal closure in *Drosophila*. *J. Cell Biol.* **149**, 471–490 (2000).
This paper is a pioneering work in the implementation of laser ablation as a tissue-stress-inference method.
179. Solon, J., Kaya-Çopur, A., Colombelli, J. & Brunner, D. Pulsed forces timed by a ratchet-like mechanism drive directed tissue movement during dorsal closure. *Cell* **137**, 1331–1342 (2009).
180. Hunter, G. L., Crawford, J. M., Genkins, J. Z. & Kiehart, D. P. Ion channels contribute to the regulation of cell sheet forces during *Drosophila* dorsal closure. *Development* **141**, 325–334 (2014).
181. Fernandez-Gonzalez, R. & Zallen, J. A. Wounded cells drive rapid epidermal repair in the early *Drosophila* embryo. *Mol. Biol. Cell* **24**, 3227–3237 (2013).
182. Campinho, P. et al. Tension-oriented cell divisions limit anisotropic tissue tension in epithelial spreading during zebrafish epiboly. *Nat. Cell Biol.* **15**, 1405–1414 (2013).
183. Maître, J.-L. et al. Asymmetric division of contractile domains couples cell positioning and fate specification. *Nature* **536**, 344–348 (2016).
184. Maître, J.-L., Niwayama, R., Turlier, H., Nédélec, F. & Hiiragi, T. Pulsatile cell-autonomous contractility drives compaction in the mouse embryo. *Nat. Cell Biol.* **17**, 849–855 (2015).
185. Yang, X. et al. Correlating cell shape and cellular stress in motile confluent tissues. *Proc. Natl Acad. Sci. USA* **114**, 12663–12668 (2017).
186. Alt, S., Ganguly, P. & Salbreux, G. Vertex models: from cell mechanics to tissue morphogenesis. *Philos. Trans. R. Soc. B Biol. Sci.* **372**, 20150520 (2017).
187. Cranston, P. G., Veldhuis, J. H., Narasimhan, S. & Brodland, G. W. Cinemechanometry (CMM): A method to determine the forces that drive morphogenetic movements from time-lapse images. *Ann. Biomed. Eng.* **38**, 2937–2947 (2010).
188. Ishihara, S. et al. Comparative study of non-invasive force and stress inference methods in tissue. *Eur. Phys. J. E Soft Matter* **36**, 9859 (2013).
189. Ishihara, S. & Sugimura, K. Bayesian inference of force dynamics during morphogenesis. *J. Theor. Biol.* **313**, 201–211 (2012).
190. Stein, M. B. & Gordon, R. Epithelia as bubble rafts: a new method for analysis of cell shape and intercellular adhesion in embryonic and other epithelia. *J. Theor. Biol.* **97**, 625–639 (1982).
One of the earliest implementations of a force-inference method applied to a cellular tissue.
191. Hayashi, T. & Carthew, R. W. Surface mechanics mediate pattern formation in the developing retina. *Nature* **431**, 647–652 (2004).
192. Chiou, K. K., Hufnagel, L. & Shraiman, B. I. Mechanical stress inference for two dimensional cell arrays. *PLoS Comput. Biol.* **8**, e1002512 (2012).
193. Brodland, G. W. et al. CellFIT: a cellular force-inference toolkit using curvilinear cell boundaries. *PLoS ONE* **9**, e99116 (2014).
194. Kong, W. et al. Experimental validation of force inference in epithelia from cell to tissue scale. *Sci. Rep.* **9**, 14647 (2019).
195. Veldhuis, J. H., Mashburn, D., Hutson, M. S. & Brodland, G. W. Practical aspects of the cellular force inference toolkit (CellFIT). *Methods Cell Biol.* **125**, 331–351 (2015).
196. Veldhuis, J. H. et al. Inferring cellular forces from image stacks. *Philos. Trans. R. Soc. B Biol. Sci.* **372**, 20160261 (2017).
197. Chen, H. H. & Brodland, G. W. Cell-level finite element studies of viscous cells in planar aggregates. *J. Biomech. Eng.* **122**, 394–401 (2000).
198. Brodland, G. W., Viens, D. & Veldhuis, J. H. A new cell-based FE model for the mechanics of embryonic epithelia. *Comput. Methods Biomech. Biomed. Eng.* **10**, 121–128 (2007).
199. Brodland, G. W. et al. Video force microscopy reveals the mechanics of ventral furrow invagination in *Drosophila*. *Proc. Natl Acad. Sci. USA* **107**, 22111–22116 (2010).
200. Sugimura, K. & Ishihara, S. The mechanical anisotropy in a tissue promotes ordering in hexagonal cell packing. *Development* **140**, 4091–4101 (2013).
201. Xu, M., Wu, Y., Shroff, H., Wu, M. & Mani, M. A scheme for 3-dimensional morphological reconstruction and force inference in the early *C. elegans* embryo. *PLoS ONE* **13**, e0199151 (2018).
202. Nestor-Bergmann, A. et al. Decoupling the roles of cell shape and mechanical stress in orienting and cueing epithelial mitosis. *Cell Rep.* **26**, 2088–2100.e4 (2019).
203. Krens, S. F. G. et al. Interstitial fluid osmolarity modulates the action of differential tissue surface tension in progenitor cell segregation during gastrulation. *Development* **144**, 1798–1806 (2017).
204. Notbohm, J., Kim, J. H., Asthagiri, A. R. & Ravichandran, G. Three-dimensional analysis of the effect of epidermal growth factor on cell-cell adhesion in epithelial cell clusters. *Biophys. J.* **102**, 1323–1330 (2012).
205. Mongera, A. et al. A fluid-to-solid jamming transition underlies vertebrate body axis elongation. *Nature* **561**, 401–405 (2018).
206. Farhadifar, R., Röper, J.-C., Aigouy, B., Eaton, S. & Jülicher, F. The influence of cell mechanics, cell–cell interactions, and proliferation on epithelial packing. *Curr. Biol.* **17**, 2095–2104 (2007).
207. Barresi, M. J. F. & Gilbert, S. F. *Developmental Biology* 12th edn (Oxford Univ. Press, 2019).

Acknowledgements
The authors apologize to the many colleagues whose work could not be cited owing to space constraints. The authors thank N. Grummel, D. Böhringer and B. Fabry for providing Fig. 2d, and A. Marin-Llauradó and T. Golde for critical reading of the manuscript. The authors are funded by the Spanish Ministry of Science, Innovation and Universities MICINN/FEDER (PGC2018-099645-B-I00 to X.T., DPI2015-71789-R to M.A.), the Generalitat de Catalunya (2017-FI-B1-00068 grant to E.L., SGR-2017-01602 grant to X.T. and 2014-SGR-1471 grant to M.A.), the CERCA Programme and ICREA Academia award (to M.A.), the European Research Council (grant CoG-616480 to X.T. and grant CoG-681434 to M.A.), the European Union's Horizon 2020 research and innovation programme (under the Marie Skłodowska-Curie grant agreement no. 797621 to M.G.-G.), Obra Social "la Caixa" and Fundació la Marató de TV3 (project 201903-30-31-32 to X.T.). The IBEC is the recipient of a Severo Ochoa Award of Excellence from the Spanish Ministry of Economy and Competitiveness (MINECO).

Author contributions
The authors contributed equally to all aspects of the article.

Competing interests
The authors declare no competing interests.

Peer review information
Nature Reviews Physics thanks U. Schwartz and C.J. Chan for their contribution to the peer review of this work.